

Composite up-conversion luminescent films containing a nanocellulose and $\text{SrF}_2\text{:Ho}$ particles

P. P. Fedorov · A. A. Luginina · S. V. Kuznetsov · V. V. Voronov ·
A. A. Lyapin · A. S. Ermakov · D. V. Pominova · A. D. Yapryntsev ·
V. K. Ivanov · A. A. Pynenkov · K. N. Nishchev

Received: 19 July 2018 / Accepted: 10 December 2018 / Published online: 8 January 2019
© Springer Nature B.V. 2019

Abstract The synthesis of up-conversion luminescent composite films based on a nanocellulose matrix containing $\text{Sr}_{1-x}\text{Ho}_x\text{F}_{2+x}$ particles was proposed. The combination of sulfuric acid hydrolysis and ultrasonication allowed us to synthesize a series of stable nanocellulose dispersions from various raw materials (powdered sulphate bleached wood pulp, Blue Ribbon filter paper, and microcrystalline cellulose Avicel). The size distribution of cellulose nanoparticles in the aqueous dispersions was

determined. Cellulose nanocrystals (CNC) and/or cellulose nanofibrils (CNF) dispersions were used to fabricate thin films by solution casting followed by solvent evaporation under ambient conditions. The size and shape of cellulose nanoparticles, surface morphology, crystallinity index of nanocellulose, polymerization degree, and optical properties were studied. By mixing aqueous dispersions of CNC with up-conversion $\text{Sr}_{1-x}\text{Ho}_x\text{F}_{2+x}$ particles, homogeneous suspensions were obtained. Finally, a solution casting technique was used to prepare CNC/ $\text{Sr}_{1-x}\text{Ho}_x\text{F}_{2+x}$ and CNC/CNF/ $\text{Sr}_{1-x}\text{Ho}_x\text{F}_{2+x}$ nanocomposite films. CNC/CNF dispersions were utilized for the production of flexible, durable, transparent composite films. The synthesized nanocomposites demonstrated intense red luminescence upon Ho^{3+} excitation by 1912 nm laser radiation. The obtained up-conversion luminescent composite films can be considered as a promising material for photonics, in particular for near-IR laser radiation visualization, luminescent labeling and luminescent sensorics.

Electronic supplementary material The online version of this article (<https://doi.org/10.1007/s10570-018-2194-4>) contains supplementary material, which is available to authorized users.

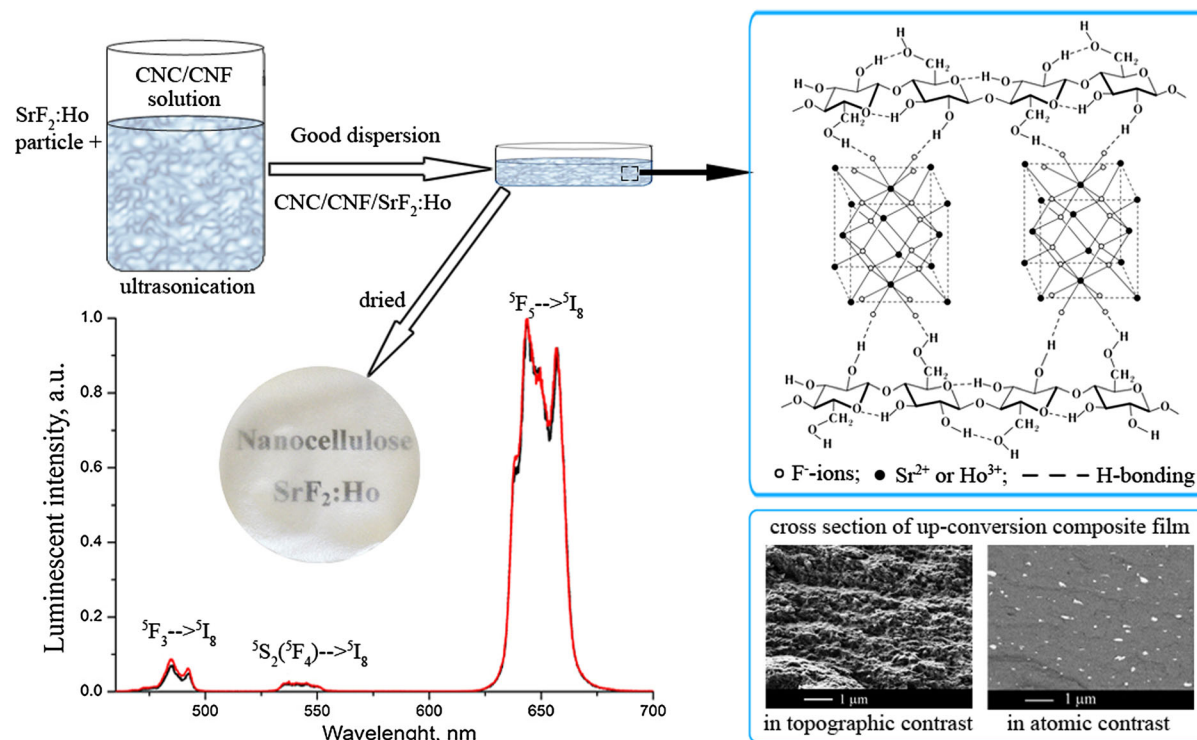
P. P. Fedorov (✉) · S. V. Kuznetsov ·
V. V. Voronov · D. V. Pominova
Prokhorov General Physics Institute of the Russian
Academy of Sciences, Vavilov str. 38, Moscow,
Russia 119991
e-mail: ppfedorov@yandex.ru

A. A. Luginina
Russian Institute for Scientific and Technical Information
(VINITI RAS), Usievicha str. 20, Moscow, Russia 125190

A. A. Lyapin · A. S. Ermakov · A. A. Pynenkov ·
K. N. Nishchev
Ogarev Mordovia State University, Bolshevistskaya str.
68, Saransk, Russia 430005

A. D. Yapryntsev · V. K. Ivanov
Kurnakov Institute of General and Inorganic Chemistry,
Leninskii Prospect 31, Moscow, Russia 119991

Graphical abstract



Keywords Cellulose nanocrystals · Cellulose nanofibrils · Nanocomposites · $\text{SrF}_2:\text{Ho}^{3+}$ · Up-conversion luminescent films

Introduction

Luminescent nanocomposites are becoming increasingly important for sensing (Zor 2018; Magyar et al. 2014; Sedov et al. 2017; Zor et al. 2018; Vicente et al. 2018) and biosensing platforms (Golmohammadi et al. 2017; Morales-Narváez et al. 2015; Dong and Roman 2007; Lin and Dufresne 2014). The use of cellulose as a matrix material has led to significantly decreased costs for sensing systems, making them easy-to-use, cheap, fast and disposable. Cellulose-based nanocomposites are used for medical diagnostics, monitoring of environmental pollution and food analysis (Li et al. 2017; Golmohammadi et al. 2017). For example, they are capable of analyzing microliter-sized liquid samples (Morales-Narváez et al. 2015; Zor 2018; Zor et al. 2018) and to measure extremely low analyte

concentrations. Various substances and materials were used as luminescent labels for nanocellulose functionalization, namely Ag and Au nanoparticles (Zor et al. 2018; Querejeta-Fernandez et al. 2015; Querejeta-Fernández et al. 2014), quantum dots (Junka et al. 2014; Xue et al. 2015; Hassan et al. 2014; Zor et al. 2018), $\text{NaYF}_4:\text{Yb}:\text{Er}$ particles with various coatings (Morales-Narváez et al. 2015; Zhao et al. 2014; Nguyen et al. 2017; Jiang et al. 2016), different organic molecules (Abbasi-Moayed et al. 2018; Dong and Roman 2007; Xue et al. 2018; Zhang et al. 2017; Lin and Dufresne 2014) and metal oxides (Nedielko et al. 2018; Shopsowitz et al. 2012; Chu et al. 2014, 2015; Zhang et al. 2018).

One of the most widely studied porous matrices for nanocomposites fabrication is nanocellulose, which possesses such advantageous properties as renewability, low toxicity, biocompatibility, biodegradability, good mechanical characteristics, pseudoplasticity, low density, good optical properties and surface reactivity (Abitbol et al. 2016). The primary building blocks of the supramolecular cellulose structure are long and thin nanosized filaments (fibrils) of 3–10 nm diameter

(Klemm et al. 2005). Nanocellulose fibrils contain highly ordered crystalline and amorphous regions, the size of crystalline regions depending on the origin of cellulose (Siro and Plackett 2010; Habibi et al. 2010). This unique cellulose structure allows separation of cellulose nanofibrils (CNF) or cellulose nanocrystals (CNC) by mechanical or chemical treatment.

The preparation and properties of nanocellulose have been considered in numerous review papers (Klemm et al. 2011; Habibi 2014; Jonoobil et al. 2015; Moon et al. 2016; Mondal 2017). CNF are typically prepared from aqueous dispersions of the original pulp by mechanical treatment, e.g. by using high-pressure homogenizers or high-intensity ultrasonicators (Eyholzer et al. 2010). Chemical or enzymatic pretreatment of cellulosic fibers is carried out to improve their dispersability (Chen et al. 2011). This type of pretreatment allows production of CNF having a diameter of about 4–10 nm (Naderi 2017). The hydrolysis process can be initiated by various reagents including hydrochloric acid (Araki et al. 2000), nitric acid (Liu et al. 2010; Cao et al. 2015), hydrochloric acid and TEMPO (Montanar et al. 2005), phosphoric acid (Espinosa et al. 2013), sulfuric acid (Martins et al. 2011; Elazzouzi-Hafraoui et al. 2008; Kim et al. 2016; Al-Dulaimi and Wanrosli 2017), tungstophosphoric acid (Hamid et al. 2016), acidic deep eutectic solvents (Sirviö et al. 2016). The hydrolysis conditions (duration, reagent concentration, temperature, cellulose source) affect the yield, morphology, diameter to length ratio, polydispersity, crystallinity index and surface charge of individual CNC (Neto et al. 2016; Beck-Candanedo et al. 2005). Controlled hydrolysis by sulfuric acid, unlike other acids, allows the sulfate groups to be grafted onto the surface of cellulose crystallites. The stability of dispersion is mainly based upon the electrostatic repulsion between negatively charged particles (Abitbol et al. 2013; Sun et al. 2016; Grishkewich et al. 2017; Niu et al. 2017).

One of the main features of cellulose is the presence of three free hydroxyls (OH^-) groups per each monomer unit which result in the highly reactive surface. As a result of hydrogen bond formation, cellulose chains are assembled into highly ordered structures (Abitbol et al. 2016; Nishiyama et al. 2002; Salas et al. 2014; Giese et al. 2015). In aqueous suspensions, cellulose nanocrystals behave as lyotropic liquid crystals with chiral nematic phase forming above the critical concentration. This structuring can

be preserved in a continuous film and cause an intense rainbow coloring (Parker et al. 2017). The ability of CNC suspensions to self-assembly to form spiral structures as well as the conservation of chiral ordering in CNC films after solvent removal determines the enormous potential for CNC in new optical material development (Ličen et al. 2016; Mu and Gray 2014; Haywood and Davis 2017; Bumbudsanpharoke et al. 2018).

CNC thin films are one-dimensional photonic crystals (Wilts et al. 2017; Giese et al. 2015). Advanced photonic materials are commonly prepared using templates ordered by a molecular self-assembly. Subsequent removal of the template allows one to obtain ordered structures with tunable spectral properties. Using CNC with a chiral nematic ordering as the templates affords fabrication of various optical devices, such as filters, sensors and optoelectronic devices (Giese et al. 2015). Selective removal of CNC template permits the formation of mesoporous carbon with a large specific surface area, large pore volume and a chiral nematic structure (Shopsowitz et al. 2011). Mesoporous silicon with metal nanoparticles embedded in the pores (Kelly et al. 2012), mesoporous TiO_2 (Shopsowitz et al. 2012), ZrO_2 and $\text{ZrO}_2/\text{Eu}^{3+}$ chiral nematic films (Chu et al. 2014, 2015), ZnS and CdS quantum dots (Hassan et al. 2014) were also synthesized by this approach.

Optical transparency and good mechanical properties of CNF films make them promising for photonics (Lavoine et al. 2012; Qing et al. 2015; Shanmugam et al. 2018; Miao et al. 2015). Similar to CNC films, CNF films can incorporate quantum dots, organic molecules and metal nanoparticles with the formation of hybrid materials (Querejeta-Fernández et al. 2014, 2015; Junka et al. 2014; Xue et al. 2015; Zhao et al. 2014; Miao et al. 2015; Xue et al. 2018, Zor et al. 2018; Zhang et al. 2017, 2018). CNF nano-paper has a strictly hierarchical structure, containing entangled nanofibrils, which are sub-structured in crystalline and amorphous domains. The influence of various interrelated parameters such as the crystallinity index, diameter to length ratio, the degree of polymerization, the colloidal stability and film formation, integration with various counterions and polymers for fibrils properties was discussed by Benítez and Walther (2017). Ji et al. (2017) for obtained transparent and flexible CNF films with high dielectric constant by Ag nanofibers incorporation. Wu et al. (2014) prepared

high-strength transparent films containing CNF and synthetic saponite nanoparticles. A facile method for highly transparent luminescent nano-paper preparation containing Eu, Sm, Tb lanthanide complexes and TEMPO-oxidized CNF was developed. Based on simple procedures, highly transparent CNF nano-paper was produced containing lanthanide complexes with high thermal stability and excellent luminescent properties (Miao et al. 2015). Chu et al. (2015) obtained chiral nematic luminescent films by incorporating $\text{YVO}_4:\text{Eu}^{3+}$ nanoparticles into CNC. Starting from nanocellulose, lightweight, elastic, thin and relatively cheap materials with sufficient mechanical strength can be produced for organic light-emitting diodes, flexible displays, photodetectors, organic solar cells and sensors (Abitbol et al. 2016; Grishkewich et al. 2017). Recently, CNC has been used as a matrix for chiral up-conversion luminescent film preparation containing $\text{NaYF}_4:\text{Yb}$, Er hexagonal nanorods. This can be judged as a new route for the development of environmentally friendly photonic bioplastics (Nguyen et al. 2017).

The up-conversion phenomenon allows one to transfer low-energy radiation pumping from the near infrared region to the visible spectral range. Generally, highly efficient luminophores are substances with low crystal lattice phonon energies, for example, metal fluorides. Non-stoichiometric inorganic fluoride phases containing rare-earth elements have attracted great scientific interest (Fedorov et al. 2011; Haase and Schäfer 2011). These up-conversion luminophores are actively studied in the form of crystalline powders (Auzel 2004; Yagoub et al. 2014, 2015), glass ceramics (Fedorov et al. 2015), and optical ceramics (Rozhnova et al. 2016). Special attention has been given to the $\text{NaYF}_4:\text{Yb}:\text{Er}$ hexagonal phase, which exhibits intense up-conversion luminescence with good quantum yields (Gu et al. 2013; Zeng et al. 2005). The highest quantum yield (10.5% at 35 W/cm² pumping) of up-conversion luminescence has been registered for $\text{NaYF}_4:21.4\% \text{Yb}^{3+}$, 2.2% Er^{3+} hexagonal phase with a micron particle size (Kaiser et al. 2017). Much less attention has been paid to up-conversion materials based on calcium fluoride and strontium fluoride doped rare-earth elements. The mechanism of up-conversion luminescence in $\text{CaF}_2:\text{Ho}^{3+}$ single crystals and laser ceramics was recently reported (Lyapin et al. 2015). A method for near-IR laser radiation visualization using $\text{Ca}_{1-x}\text{Ho}_x\text{F}_{2+x}$

powders was also recently proposed (Lyapin et al. 2017). SrF_2 is a more suitable matrix for optical applications than CaF_2 due to even lower phonon energies and suppression of non-radiative relaxation (Ritter et al. 2016). High-efficiency up-conversion phosphors based on $\text{SrF}_2:\text{Yb}:\text{Er}:\text{Tm}$ (Rozhnova et al. 2014; Pak et al. 2017), $\text{SrF}_2:\text{Yb}:\text{Er}$ (Rozhnova et al. 2016; Kuznetsov et al. 2018) and $\text{SrF}_2:\text{Er}:\text{Ho}$ (Lyapin et al. 2017) were proposed recently. Nanocellulose matrix-based composite materials with $\text{SrF}_2:\text{Ho}$ up-conversion particles are promising luminescent materials for infrared radiation imaging in medicine, lighting, and laser spectroscopy. Thus, it is important to develop simple and affordable synthetic methods for the luminescent composite nanocellulose-containing materials having uniformly distributed components and tunable properties. Thus, the aim of this paper is the synthesis and investigation of nanocrystalline or nano-fibrillated cellulose-based polymer-inorganic composite films containing $\text{SrF}_2:\text{Ho}$ up-conversion particles.

Experimental section

Materials

Microcrystalline cellulose (Avicel PC-105 from FMC BioPolymer Corporation, Philadelphia, USA), powdered bleached woodkraft cellulose (PCC-0.25 (PC) from Polycell, Vladimir, Russia), filter paper “Blue Ribbon” (FP), 98% sulfuric acid, double distilled water, regenerated cellulose dialysis tubing with 12–14 kDa molecular weight cut-off from Orange Scientific (Graigette Business Park, Braine-l’Alleud, Belgium) and $\text{Sr}_{1-x}\text{Ho}_x\text{F}_{2+x}$ ($x = 0.08$ and 0.10) up-conversion powders prepared by recently proposed technique (Fedorov et al. 2017) were used as starting materials. The characteristics of the Avicel, PC and FP cellulose samples are given in Table 1.

Preparation of cellulose nanocrystals (protocol #1)

Initial PC and FP cellulose samples were mixed with double distilled water (cellulose:H₂O ratio = 1:10 g/g) in a lab glass. FP sample was preliminarily shredded to small pieces (about 2 × 2 mm). The prepared suspension was placed in an ice bath. Concentrated sulfuric acid (cellulose:H₂SO₄ ratio = 1:25 g/g) was

Table 1 The properties of initial cellulose samples (see also Figs. S1, S2, S3 in Supplementary Information for details)

Initial cellulose sample	Particle size (SEM) (μm)		Cellulose structure	IC (%)	DP	Decomposition temperature [$T_{\text{onset}}/T_{\text{endset}}$ ($^{\circ}\text{C}$)]
	Width	Length				
Avicel	3–10	10–40	I β	78.5	197	291/543
PC	25–50	230–500	I β	69.2	930	300/491
FP	25–50	200–1500	I β	68.7	1112	300/486

IC crystallinity index, DP degree of polymerization

added dropwise to the cellulose suspensions under mechanical stirring until acid concentration reached approximately 65 wt%. Then, the resulting suspension was placed in a water bath at 47 $^{\circ}\text{C}$ for 60 min under 350 rpm stirring. Hydrolysis was terminated by addition of 10-fold excess of cold double distilled water. The hydrolyzed suspension was washed with double distilled water and repeatedly centrifuged (Eppendorf 5804 centrifuge, 8000 rpm, 10 min). The supernatant was separated from the precipitate and then a new portion of water was added. After 4–5 centrifugation cycles, washing procedure was terminated at pH = 4. The resulting cellulose gel was dispersed in double distilled water and then placed into a dialysis bag and dialyzed for 7 days. The diluted suspension was further dialyzed to remove residual acid and other low molecular weight materials until a pH of 5.5 was reached. After dialysis, the dispersion was sonicated for 15 min (UZG13-01/22 sonicator, 110 W, VNIITVCH) in an ice bath. The yield of CNC was about 30%.

Aq. 65% sulfuric acid was added to the Avicel powder with subsequent stirring at 47 $^{\circ}\text{C}$ for 30 min (Avicel:H₂SO₄ ratio = 1:25 g/g). The next steps were the same as described above. The yield of CNC was ~ 30% in this case.

The resulting CNC from various cellulose samples are hereafter designated as CNC_{PC}, CNC_{FP}, CNC_{AV}.

Preparation of cellulose nanofibrils (protocol #2)

CNF samples were obtained by combining preliminary chemical treatment of initial cellulose samples with long-term ultrasonication. 50% sulfuric acid was added to Avicel or PC sample under stirring (Avicel:H₂SO₄ ratio = 1:12 g/g, PC:H₂SO₄ ratio =

1:13 g/g) at 45 $^{\circ}\text{C}$ for 60 min. FP was preliminarily shredded into small pieces ($\sim 2 \times 2$ mm). FP sample was then mixed with double distilled water (FP:H₂O ratio = 1:10 g/g). Concentrated sulfuric acid (FP:H₂SO₄ ratio = 1:13 g/g) was added dropwise under stirring to the slurry placed in an ice bath. The resulting suspension was placed in a water bath at 45 $^{\circ}\text{C}$ for 60 min (350 rpm). The hydrolysis was terminated by adding a large amount of cold double distilled water (10 times the volume of the suspension). The suspension was then washed with double distilled water and repeatedly centrifuged (10 min at 8000 rpm, an Eppendorf 5804 centrifuge). The supernatant was separated from the precipitate and then a new portion of water was added. After 4–5 centrifugation cycles, washing was terminated at pH 4. The aqueous suspension was then sonicated in an ice bath for 30 min (UZG13-01/22 sonicator, 110 W, VNIITVCH). Suspension was dispersed in double distilled water and further dialyzed for 7 days. After dialysis, the suspension was sonicated according to the above-mentioned procedure. The yield of CNF was about 50%.

The resulting cellulose nanofibrils samples are hereafter designated as CNF_{PC}, CNF_{FP}, CNF_{AV}.

Preparation of nanocellulose films

The preparation of nanocellulose films is based on solution casting on a plastic substrate followed by solvent evaporation under ambient conditions. Briefly, a pre-determined amount of the CNC or CNF colloidal suspension with concentration less than 3 wt% was poured into polystyrene Petri dishes followed by drying under ambient conditions for 3–4 days. After evaporation of the excess of solvent, formed CNC or

CNF films were carefully separated from the plastic substrate as a self-standing structure. The film thickness was $\sim 20\text{--}25\ \mu\text{m}$.

Preparation of nanocomposites films

$\text{Sr}_{1-x}\text{Ho}_x\text{F}_{2+x}$ powders ($x = 0.08$ and 0.10) annealed at $750\ ^\circ\text{C}$ were carefully ground in an agate mortar. Then the powders were dispersed in CNC or CNF colloidal solutions by sonication on an ice bath for 15 min. The resulting slurries were stirred for 30 min at room temperature by a magnetic stirrer. The colloidal suspensions were poured into polystyrene Petri dishes and dried under ambient conditions for 3–4 days. The air-dried composite films were further dried at $85\ ^\circ\text{C}$ for 40 min to remove residual moisture, so the latter would not affect morphology, physical and luminescent characteristics. The film thickness was $\sim 25\text{--}30\ \mu\text{m}$. The nanocellulose content in the dried films varied from 45 to 90 wt%, while the Ho content in the dried films ranged from 1.00 to 6.71 wt%. The composite films were designated as CNC:xHo, CNF:xHo, CNC/CNF:xHo, where $x = \text{Ho wt\%}$.

Characterization methods and equipments

X-ray diffraction analysis of the samples was carried out on a Bruker D8 Advance diffractometer (Bruker AXS GmbH, Karlsruhe, Germany) using $\text{CuK}\alpha$ -radiation in the range $8^\circ\text{--}60^\circ\ 2\theta$. Samples were of the I β cellulose structural type. The diffraction peak at $22.7\ 2\theta$ was used for crystallinity index (IC, %) calculation by Segal's method according to Eq. (1):

$$IC = \frac{I_{200} - I_{AM}}{I_{200}} \times 100, \quad (1)$$

here I_{200} is the intensity of the $\langle 200 \rangle$ reflex at $22.70\ 2\theta$, I_{AM} is the intensity at the minimum between the $\langle 200 \rangle$ and $\langle 110 \rangle$ peaks at $18.00\ 2\theta$.

X-ray diffraction data were collected in reflection geometry. In this geometry, the incident radiation is most intensively scattered by crystallites whose reflecting planes are parallel to the axis of the fibrils. The latter reason allows determination of their thickness. Coherent scattering domains sizes ($D[200]$, nm) were calculated by the Scherer Eq. (2):

$$D[200] = \frac{k\lambda}{\beta[200] \cos \theta}, \quad (2)$$

here $D[200]$ is coherent scattering domains size, $k = 0.94$ is Scherer constant for cellulose, λ is X-ray wavelength ($0.155418\ \text{nm}$), $\beta[200]$ is the total width of the diffraction peak at half-height, θ —Bragg angle (Nam et al. 2016; Lee et al. 2017).

The nanoparticle size distribution in aqueous dispersions was determined by dynamic light scattering (DLS) using a Photocor Complex DLS spectrometer equipped with He–Ne laser. The CNC and CNF dispersions were preliminarily diluted up to 0.1 wt% concentration and then ultrasonicated for 5 min in an ice bath. The average degree of polymerization (DP) was measured by the viscosity method using diluted solutions of dry cellulose particles in Cadoxen (cadmium ethylenediamine) (Ioelovich 2012). The polymerization degree was determined as the average of two independent measurements. The relative error was 4% at $p = 0.95$.

Film thickness was measured using a micrometer (MKTS-25 0.001, Kalibron, Russia) at seven randomly selected locations on each film, and mean value was reported for each replication.

The microstructure of the powders and films was analyzed by scanning electron microscopy (SEM) using a NVision 40 microscope (Carl Zeiss NTS GmbH, Oberkochen, Germany) with simultaneous energy-dispersive spectroscopy (EDX) (X-Max detector, Oxford Instruments, Abingdon, UK).

Fourier transform infrared spectroscopy (FTIR) was performed on a INFRALUM FT-08 spectrometer from 400 to $4000\ \text{cm}^{-1}$. The transmission spectra were recorded using a Cary 5000 spectrophotometer in the $250\text{--}3000\ \text{nm}$ range.

Differential scanning calorimetry (DSC) was performed on a Netzsch DSC 404 F1 Pegasus. Thermal gravimetric analysis (TG) was performed from 25 to $800\ ^\circ\text{C}$ with a $5\ ^\circ\text{C}/\text{min}$ heating rate in air using a Netzsch TG 209 F1 Libra calorimeter.

The up-conversion luminescence spectra were recorded with a Horiba FHR 1000 spectrophotometer. A continuous solid-state $\text{LiYF}_4:\text{Tm}$ laser was used as the excitation source for Ho^{3+} ions at $1912\ \text{nm}$. The beam diameter of incident laser radiation was $300\ \mu\text{m}$.

Results and discussion

CNC and CNF investigation

SEM images of CNC_{AV} and CNC_{PC} samples indicated the presence of randomly located rod-shaped particles

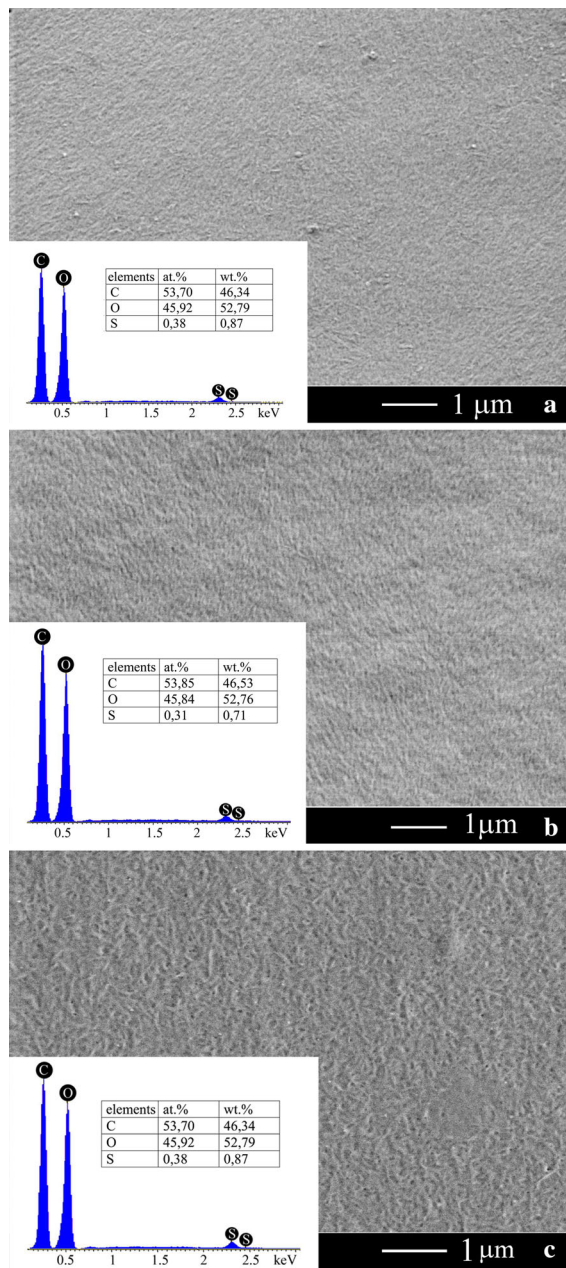


Fig. 1 SEM images of dispersions of CNC on a carbon substrate (concentration 0.1 wt%): **a** CNC_{AV} , **b** CNC_{PC} , **c** CNC_{FP} ; the insets present EDX data

having widths of 10–20 nm and lengths of 100–200 nm (Fig. 1a, b), as well as aggregates of these particles. There is no noticeable difference between these two samples. For CNC_{FP} sample, the particle size is larger, with widths of 10–25 nm and lengths of 140–250 nm (Fig. 1c).

The insets show the quantitative results of EDX analysis of different CNC samples (Fig. 1a–c). The presence of sulfur is due to the esterification of cellulose hydroxyl groups by sulfate ions. The presence of sulfate groups ensures stable aqueous dispersion formation. Our data are in a good agreement with previously reported results (Beck-Candanedo et al., 2005; Abitbol et al., 2013). Thus the optimized one-stage acid hydrolysis procedure results in the formation of CNC samples having similar morphology and particles sizes. The duration of Avicel hydrolysis is half that of PC and PP hydrolysis. Particle sizes determined by SEM are in good agreement with DLS results (Fig. 2a–c). Hydrodynamic particle radii for all types of CNC follow bimodal particle distributions. Two groups of particles can be distinguished: CNC_{AV} and CNC_{PC} — 8 ± 1 nm and 120 ± 37 nm, CNC_{FP} — 9 ± 1 nm and 190 ± 52 nm.

As a result of the hydrolysis, the particle sizes in the CNC_{AV} aqueous dispersion are reduced by approximately two orders of magnitude in comparison with the source material. The CNC_{PC} and CNC_{FP} particle sizes are approximately three orders of magnitude smaller than the particle sizes in original PC and FP samples. The sample obtained from Avicel according to procedure 2 comprises different particles (Fig. 3a): rod-shaped nanoparticles (25–50 nm in thickness and 140 nm in length), longitudinally connected head–tail nanoparticles up to 430 nm in length and a small number of cellulose microparticles (140–240 nm thickness, 570–1400 nm length). This sample is not nanofibrillized cellulose, it was marked as NC_{AV} . The initial Avicel sample is characterized by a high IC (78.5%), which is typical for a high crystalline phase content. Avicel hydrolysis using a lower sulfuric acid concentration (50%) with simultaneous ultrasonic treatment was accompanied by the destruction of amorphous and crystalline part of cellulose fibrils. This is confirmed by a decrease in the crystallinity index of NC_{AV} , as determined by further studies.

SEM images of PC and FP samples obtained by technique 2 (Fig. 3b, c) show CNF particles with anisotropic shape (20–32 nm width, from 200 to

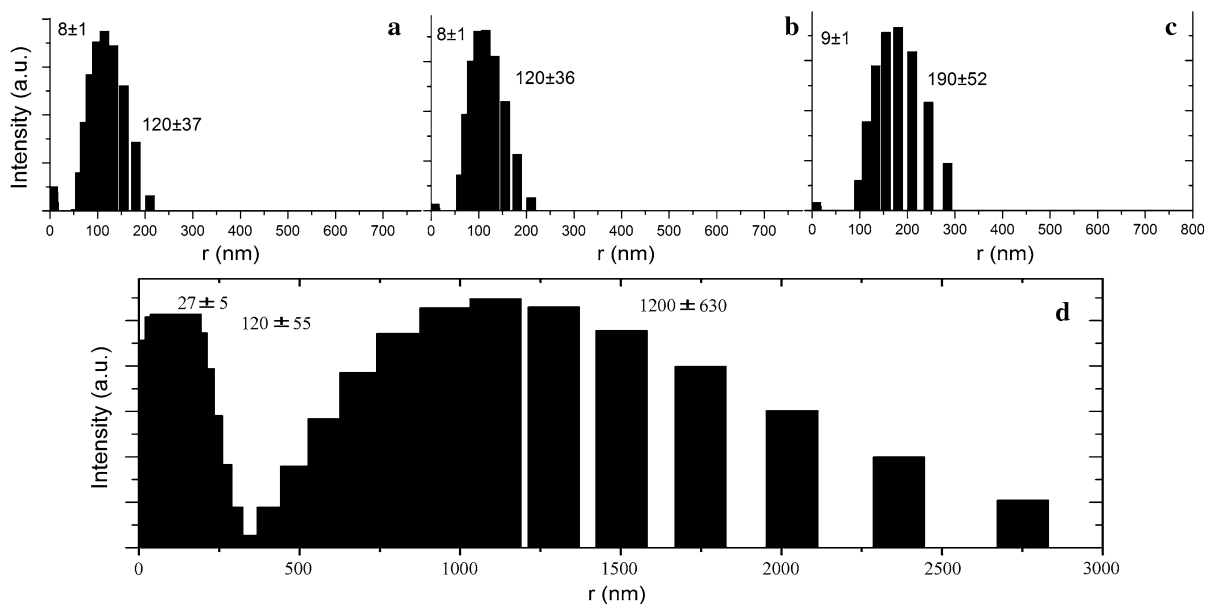


Fig. 2 Particle size distributions in dilute aqueous nanocellulose dispersions (concentration 0.1 wt%) determined by DLS: **a** CNC_{AV}, **b** CNC_{PC}, **c** CNC_{FP}, **d** CNF_{PC}

2000 nm length). These particles have a large aspect ratio (20–60), which confirms the nano-fibrillated cellulose preparing. Entangled CNF fibrils form a porous network. Hydrolysis of the original cellulose with 50% sulfuric acid was unable to produce nanocrystals. When using 50% sulfur acid with simultaneous ultrasonic treatment, long fibrils some amorphous regions were formed. A similar effect was reported previously (Al-Dulaimi and Wanrosli 2017). DLS data together with SEM/EDX data reveal poly-disperse particle size distributions for CNF_{PC} and CNF_{FP} samples with maxima at 22–32, 90–200 and 500–2000 nm (Fig. 2d). According to EDX analysis, the sulfur content in CNF samples (0.05–0.07 wt%) is lower than that in CNC samples. This can be explained by a smaller excess of H₂SO₄, a lower acid concentration, and prolonged ultrasonication. Although the dispersions were cooled in an ice bath during sonication, temperature rise, especially localized, can not be completely ruled out. This can cause hydrolysis of the sulfate groups on CNF surface and reduce the sulfur content and the surface charge of the particles (Beck-Candanedo et al. 2005).

The resulting CNC aqueous dispersions of 1.60–2.39 wt% concentration are stable colloidal solutions of nanocrystalline cellulose, showing no coagulation for three months or more (Fig. S4a). The

stability of CNC dispersions is supposedly caused by the presence of negatively charged sulfate groups on the CNC surface increasing the surface charge on the CNC particles. This results in CNC dispersion stabilization due to electrostatic repulsion between sulfate groups (Sun et al. 2016; Al-Dulaimi and Wanrosli 2017).

The 0.94–1.67% CNF_{PC} and CNF_{FP} dispersions are milky in color and stable for 3 weeks (Fig. S4b). After 3 weeks, the dispersion began to separate into two layers. The 2.21 wt% NC_{AV} aqueous dispersion is stable for 1 week, then particle aggregation and precipitation occurs.

The conclusion about the stability limit of the isotropic phase as 3 wt% (2 vol%) for 100 nm long and 7 nm wide sulfated CNC (Oguzlu et al. 2017) did not contradict to our results for the CNC aqueous dispersions stability.

In our study, the morphology, particle size, aspect ratio of the particles, degree of polymerization, and crystallinity index of nanocellulose depend mainly upon the preparation technique in turn. The cellulose source used in our work had a negligible effect on the nanocellulose properties. Our analysis indicates that the tightening of the hydrolysis conditions such as raising the acid concentration increasing the stoichiometry of the acid and increasing the hydrolysis

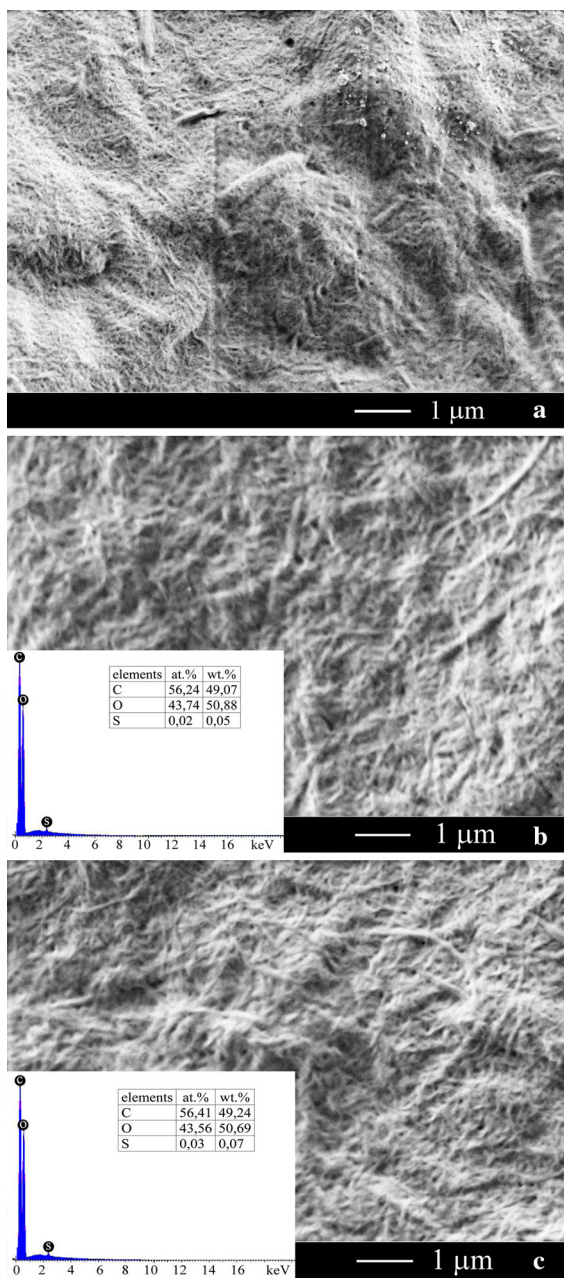


Fig. 3 SEM images of diluted dispersions (concentration 0.1 wt%) dried on a carbon substrate: **a** NC_{AV} , **b** CNF_{PC} , **c** CNF_{FP} ; the insets present the EDX data

temperature lead to the rupture of the polymer chains in amorphous cellulose regions. This results in a decrease in the polymerization degree and a increase crystallinity index of samples.

Investigation of CNC and CNF films

Changes in the supramolecular structure of cellulose films at different hydrolysis stages were traced by XRD. For all nanocellulose samples, the $I\beta$ monoclinic structure was retained (Fig. 4).

Two broad peaks typical for nanocellulose can easily be observed, one with a blurred maximum at 15.0–16.5 2θ , and the second with maximum at 22.5 2θ (Fig. 4a–f). In addition to these peaks, there are also several peaks related to $Sr_{1-x}Ho_xF_{2+x}$ solid solution (Fig. 4g–h). XRD patterns of initial Avicel, PC and FP cellulose samples show reflexes at 14.9, 16.5, 22.4 and 34.40 2θ (Fig. S2). These lines with indices ($\bar{1}10$), (110), (200) and (004), are characteristic for $I\beta$ cellulose (Feng et al. 2015).

Crystallinity indices, calculated according to the Eq. 1, are presented in Table 2.

CNC samples show a significant raise for the crystallinity indices as compared to the original cellulose (Table 1) as a result of the optimized acid hydrolysis treatment. Crystallinity indices increased from 78.5%, 69.2%, 68.7% to 86.5%, 86.0%, 84.6% for CNC_{AV} , CNC_{PC} , and CNC_{FP} , respectively. The increase in the crystallinity indices for CNF_{PC} and CNF_{FP} occurred with the partial destruction of an amorphous part of cellulose due to an insufficient quantity acid at pre-chemical treatment stage before sonication. A slight decrease in the crystallinity index from 78.5% (Avicel) to 76.7% (NC_{AV}) was noted. All

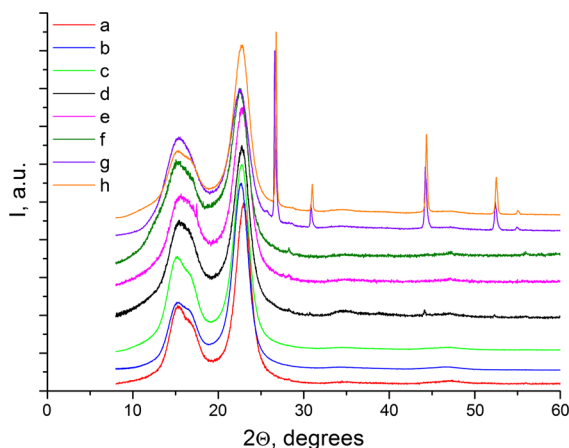


Fig. 4 XRD data: (a) CNC_{AV} , (b) CNC_{PC} , (c) CNC_{FP} , (d) NC_{AV} , (e) CNF_{PC} , (f) CNF_{FP} , (g) CNC_{FP} :1.1 wt% Ho, (h) CNC_{PC} :2.2 wt% Ho

Table 2 The characteristics of nanocellulose samples prepared using different sources

Sample	Particle size (SEM) (nm)		Cellulose structure	IC (%)	L (nm)	DP	Decomposition temperature [$T_{\text{onset}}/T_{\text{endset}}$ (°C)]
	Width	Length					
CNC _{AV}	10–20	100–200	Iβ	86.5	4.0	76	155/515
CNC _{PC}	10–20	100–200	Iβ	86.0	3.9	106	155/514
CNC _{FP}	10–25	140–250	Iβ	84.6	3.9	118	157/514
NC _{AV}	25–50	140–430	Iβ	76.7	3.7	149	184/586
CNF _{PC}	22–32	200–2000	Iβ	75.7	3.5	140	196/591
CNF _{FP}	22–32	200–2000	Iβ	69.2	3.3	154	186/556

of the NC_{AV} films were cracked and crumbled prior to drying.

The average cross-sectional dimensions of CNC elementary crystallites, calculated using the Scherrer equation is 3.9–4.0 nm, which is consistent with earlier reports (Elazzouzi-Hafraoui et al. 2008; Beck-Candanedo et al. 2005; Lee et al. 2017). The cross-section dimensions of the crystallites are 3.5 nm for CNF_{PC} and 3.3 nm for CNF_{FP}.

The polymerization degree was significantly reduced upon hydrolysis, especially for FP (by 9.4-fold), PC (by 8.8-fold) and AV (by 2.6-fold). CNC has a 1.3-fold lower polymerization degree than CNF. The DP = 76 was the lowest value for CNC_{AV}. The length of the elementary link of the cellulose macromolecule was 5.2 Å (Ioelovich, 2016). The length of the CNC_{AV} macromolecule was 40 nm. According to SEM data, the CNC_{AV} particle lengths (Fig. 1a) was 100–200 nm. Here, the CNC_{AV} particles consisted of 3–5 cellulose macromolecules.

The different shape and length of CNC and CNF particles affect their behavior during film formation. SEM images of the CNC and CNF films are shown in Fig. 5. CNC tends to form ordered structures (Fig. 5a, c, d). This phenomenon can be associated with CNC self-assembly during drying (Pan et al. 2010; Park et al. 2014). SEM images of CNC_{AV} and CNC_{FP} films (Fig. 5a, d) demonstrated spontaneous orientation of the rod-like cellulose nanoparticles. Spontaneous orientation of CNC_{PC} rod-like particles is clearly visible in Fig. 5c. In turn, entangled CNF nanofibrils formed a porous network (Fig. 5e). Aggregated rod-like nanocrystals are located on the surface of CNC/CNF films (Fig. 5f).

Self-assembly upon gentle drying of CNC_{AV} and CNC_{PC} dispersions led to the formation of transparent iridescent and brittle films (Fig. 6a, b). Chiral nematic or cholesteric structures in the anisotropic phase consisted of superposed planes formed by elongated CNC rod-like particles in one direction. For both CNC dispersions and films, only a left-handed chiral structure was demonstrated (Gray 2016; Gray and Mu 2015; Liu et al. 2014; Tardy et al. 2017; Dumanli et al. 2014). CNC_{AV} film cross section (Fig. 5b) proves the left-handed chiral nematic structure of this samples (Parker et al. 2017; Frka-Petesic et al. 2017). The gradual removal of the aqueous phase upon evaporation lead to a mutual arrangement of cellulose nanocrystals by minimizing the existing electrostatic interactions. In this manner, homogeneous concentrated suspensions are self-organized into liquid crystal structures. In 1998, the first demonstration was reported for the chiral nematic structure in nanocrystalline cellulose films upon evaporation of the solvent in the EISA process (evaporation-induced self-assembly) (Revol et al. 1998). Obviously, the iridescent color of CNC_{AV} (2.10 wt% dispersion) and CNC_{PC} (2.39 wt% dispersion) films is associated with chiral nematic structure formation at dispersion concentrations higher than 1.60 wt% CNC_{FP}. The CNC_{FP} film is transparent, colorless and less brittle than CNC_{AV} and CNC_{PC} iridescent films (Fig. 6c). The concentration of CNC_{FP} dispersion is not sufficient for chiral nematic structure formation upon water evaporation during the film drying.

The presence of entangled nanofibers makes it much easier to form a porous network (Fig. 5e). A flexible and wrinkled film with a milky shade is formed when using 0.94 wt% CNF_{PC} dispersion

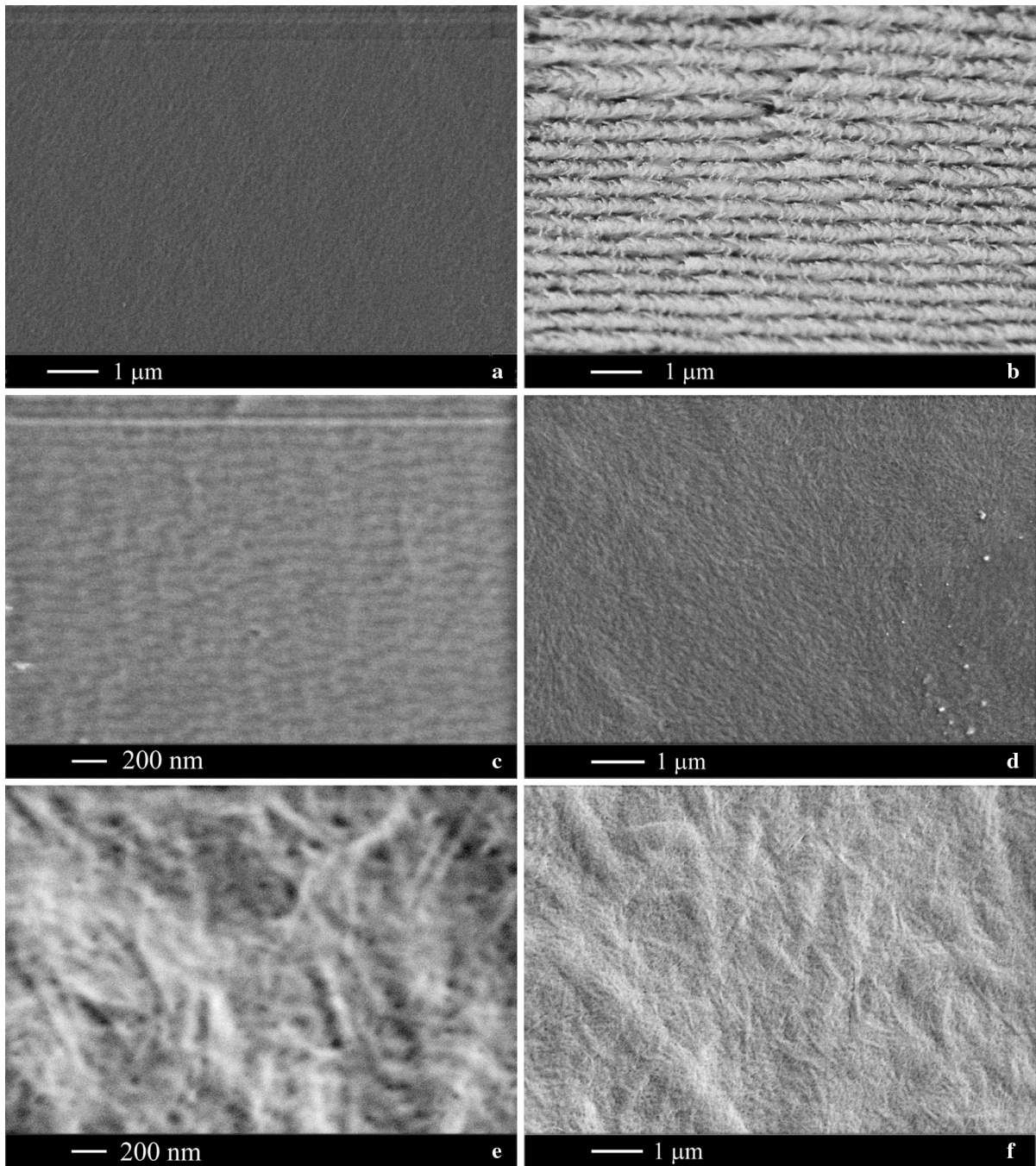


Fig. 5 SEM images of cellulose films: **a** CNC_{AV} , **b** SEM cross sections of CNC_{AV} , **c** CNC_{PC} , **d** CNC_{FP} , **e** CNF_{PC} , **f** $\text{CNC}_{\text{PC}}/\text{CNC}_{\text{FP}}$ (1:1) samples

(Fig. 6d). When the dispersion concentration was increased to 2.07 wt%, a nearly non-transparent film was formed (Fig. 6e). Thus, various mechanisms for

CNC and CNF films formation affect their optical and mechanical properties.

Mixed CNC/CNF films were obtained to improve their flexibility. Before film preparation, aqueous



Fig. 6 Appearance of cellulose: **a** CNC_{AV}, **b** CNC_{PC}, **c** CNC_{FP}, **d** CNF_{PC} (0.94 wt%), **e** CNF_{FP} (2.07 wt%), **f** mixed film CNC_{PC}:CNC_{FP} = 1:1

CNC/CNF dispersions were sonicated in an ice bath for 15 min with 3-min intervals for every 5 min. The best combination of mechanical characteristics (strength and flexibility), optical and thermal properties was obtained for the 1:1 CNC:CNF film. SEM data for CNC:CNF film are shown in Fig. 5f. The microstructure of the mixed CNC:CNF film is nearly the same as for CNF films. Obviously, CNC is evenly distributed within the CNF matrix. This is due to the high compatibility between CNF and CNC having the same chemical structure. The CNC homogeneous dispersion inside the CNF matrix improves the optical transparency in comparison with pure CNF films, as well as the heat resistance and mechanical properties of pure CNC films. The mixed films are transparent, colorless, and flexible without cracks (Fig. 6f).

The transparency and color of the films were analyzed by the transmission UV–Vis spectroscopy (Fig. 7).

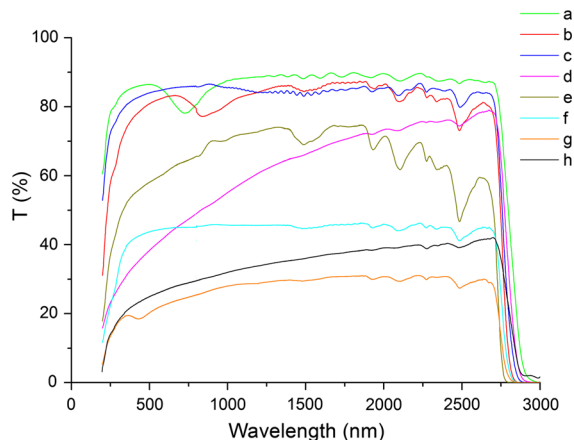


Fig. 7 Transmission spectra of cellulose films: **(a)** CNC_{AV}, **(b)** CNC_{PC}, **(c)** CNC_{FP}, **(d)** CNF_{PC}, **(e)** CNC_{PC}/CNC_{FP} = 1/1, **(f)** CNC_{FP}:1.1 wt% Ho, **(g)** CNC_{PC}:5.4 wt% Ho, **(h)** CNC_{PC}/CNF_{FP}:5.6 wt% Ho

Transmission at 650 nm wavelength for CNC films is as high as 83% (Fig. 7a–c). The transmission spectra of CNC_{AV} and CNC_{PC} films contain a weak absorption band in the 700–770 nm range, which is associated with the film’s iridescent color. The transmission of CNF films is lower than that of CNC films (about 45% at 650 nm), depending on the filler content (Fig. 7d). The transmission of mixed CNF/CNC films (62% at 650 nm) is higher than that of CNF films and slightly lower compared to CNC films (Fig. 7e).

Transparency of the films is an important factor for practical applications. The combination of physical and chemical properties of CNC and CNF make them attractive for smart photonic devices, sensors (Dai et al. 2017), color filters (Bumbudsanpharoke et al. 2018), iridescent mesoporous cellulose membranes with adjustable colors, and biosensors (Dumanli et al. 2014).

The thermal degradation of the Avicel, PC, FP cellulose sample and CNC and CNF samples derived from these precursors proceeds in different ways. The initial and final decomposition temperatures (T_{onset} and T_{endset}) are presented in Tables 1 and 2, the DSC and TG curves are shown in Figs. S3 and 8. T_{onset} is reduced by almost 100 °C, and by 140 °C for CNF as compared to the original cellulose.

The decrease of the thermal stability of CNC and CNF was probably associated with an increase in the heat exchange rate due to the surface area increase, smaller particle sizes and the presence of sulfate

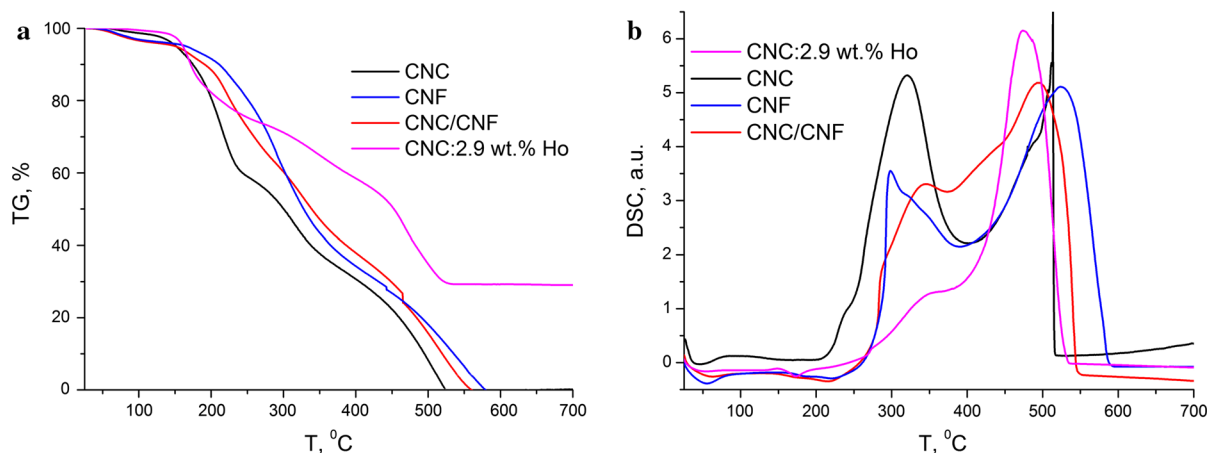


Fig. 8 DSC and TG curves: **a** TG and **b** DSC for CNC_{PC}, CNF_{PC}, CNC_{PC}/CNF_{FP} (1:1) and CNC_{PC}:2.9 wt%:Ho films

groups. Sulfate groups act as a catalyst during the thermal decomposition of cellulose (Al-Dulaimi and Wanrosli 2017). Thermal behavior for CNF films prepared from different cellulose sources are depicted in Fig. 8a, b. CNC films also show a similar behavior upon heating while their decomposition proceeds at lower temperatures comparing to CNF films (Fig. 8a, b). The decrease in the CNC films' thermal destruction temperature due to the influence of sulfate groups has been thoroughly studied recently (Sun et al. 2018). We believe that the lower temperatures (T_{onset}) for thermal decomposition (155–157 °C) of CNC films are due to the higher content of sulfate groups that is evidenced by EDX data. The difference in morphology for CNF and CNC films could also be affected by the thermal destruction process. The CNC surface area is larger than that of CNF due to the smaller nanoparticle size. The DSC and TG curves show that the thermal destruction of CNF films in the air begins at 186–196 °C with an endothermic effect at 215 °C (Fig. 8b). Destruction of CNC films begins at a lower temperature (157 °C) with an endothermic effect at 205 °C (Fig. 8b). The endothermic effect corresponds to the first stage of the cellulose decomposition process, which is catalyzed by sulfate groups. The DSC curves also have two exothermic effects at 338 °C and 526 °C for CNF, and 314 °C and 514 °C for CNC. The first exothermic effect indicates the beginning of the cellulose oxidation. The second exothermic effect corresponds to CO₂ and H₂O formation, which ends at 591 °C and 514 °C for CNF and CNC, respectively. The TG curves are of a

multi-stage type. The first stage is the removal of physically bound water (~ 80–110 °C) with a weight loss of 2.3–2.8% and 3.3–3.6% for CNC and CNF films, respectively. The difference between TG-curves for CNC and CNF films in the presence of the additional stage at 210 °C and a substantial weight loss (37%) in the 110–210 °C region for CNC. The weight loss for CNC is significantly higher (7%) than for CNF in the same temperature range. This fact confirms the abovementioned opinion about influence of the sulfate groups content on the nanocellulose thermal decomposition. The total weight loss for all the samples is 100%. Mixed 1:1 CNF/CNC films demonstrate increased thermal stability as compared to CNC: their thermal degradation starts at 170 °C and ends at 550 °C.

The IR spectra of CNC_{PC}, CNF_{PC} and CNC_{PC}:5.4 wt% Ho films contained absorption bands at 2900 cm⁻¹ (stretching modes of CH- and CH₂-groups), 1650 cm⁻¹ (stretching modes of C=O bond), 1430 cm⁻¹ (symmetric deformation vibrations of CH₂ group), 1000–1200 cm⁻¹ (stretching modes of C–O–C and C–O bonds in the pyranose rings) (Fig. 9). The CNC IR spectrum contained an additional weak band at 1231 cm⁻¹ (S=O), which confirmed the sulfate group introduction into cellulose structure during hydrolysis (Al-Dulaimi and Wanrosli 2017). CNC and CNF samples were characterized by a broad absorption band at 3225–3505 cm⁻¹ and 3275–3455 cm⁻¹ regions. These bands corresponded to the stretching modes of OH-groups. For the CNC composite film with 5.4 wt% Ho, the band at

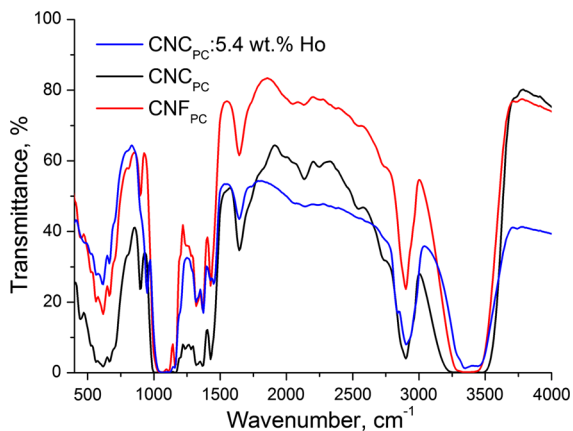


Fig. 9 IR spectra of CNC, CNF and CNC:5.4 wt%Ho composite films

3350–3450 cm^{-1} became narrow and slightly shifted to higher wavenumbers in comparison to pure CNC. This can be explained by hydrogen bond formation between OH^- groups in CNC and F^- ions in $\text{Sr}_{0.92}\text{Ho}_{0.08}\text{F}_{2.08}$ particles.

Spectral and luminescent properties of $\text{Sr}_{1-x}\text{Ho}_x\text{F}_{2+x}$ powders

$\text{Sr}_{1-x}\text{Ho}_x\text{F}_{2+x}$ ($x = 0.08$ and 0.10) powders emit predominantly in red visible range at 1912 nm laser pumping of $^5\text{I}_7$ Ho^{3+} level. The up-conversion luminescence spectra of $\text{Sr}_{0.92}\text{Ho}_{0.08}\text{F}_{2.08}$ and $\text{Sr}_{0.90}\text{Ho}_{0.10}\text{F}_{2.10}$ powders are shown in Fig. 10.

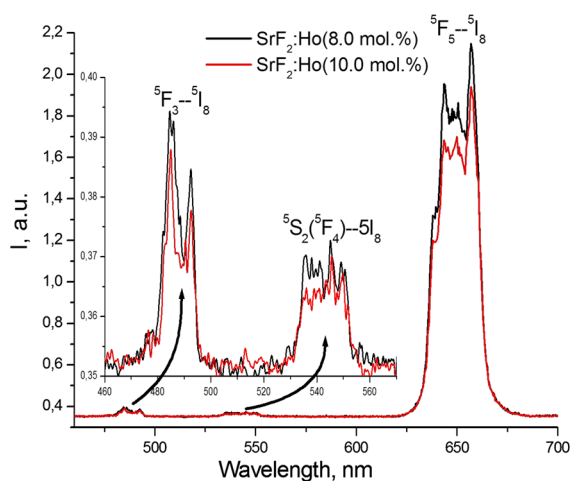


Fig. 10 Up-conversion luminescence spectra of $\text{Sr}_{0.92}\text{Ho}_{0.08}\text{F}_{2.08}$ and $\text{Sr}_{0.90}\text{Ho}_{0.10}\text{F}_{2.10}$ powders

The intensity of $\text{Sr}_{1-x}\text{Ho}_x\text{F}_{2+x}$ ($x = 0.08$ – 0.10) up-conversion luminescence was measured for the samples calcined at 750 °C (Fedorov et al. 2017). The luminescence intensity for a concentration of 10 mol% of holmium is similar to 8 mol%. $\text{Sr}_{0.92}\text{Ho}_{0.08}\text{F}_{2.08}$ and $\text{Sr}_{0.90}\text{Ho}_{0.10}\text{F}_{2.10}$ powders can be used as visualizers of two-micron laser radiation. Thus, powders were used as an up-conversion filler in the preparation of composite films made from nanocellulose.

Composite films based on CNC and CNF with $\text{SrF}_2:\text{Ho}$ up-conversion powders

CNC dispersion and $\text{Sr}_{0.92}\text{Ho}_{0.08}\text{F}_{2.08}$ or $\text{Sr}_{0.90}\text{Ho}_{0.10}\text{F}_{2.10}$ powders were mixed with subsequent ultrasonic treatment. This results in a good distribution of the powders in the CNC matrix (Fig. S4c, d). Transparent and stable CNC dispersions were obtained with 0.40–1.92 wt% up-conversion powders. X-ray diffraction patterns of composite films containing $\text{CNC}_{\text{FP}}/10.9$ wt% $\text{Sr}_{0.92}\text{Ho}_{0.08}\text{F}_{2.08}$ ($\text{CNC}_{\text{FP}}:1.1$ wt% Ho) or $\text{CNC}_{\text{PC}}/21.9$ wt% $\text{Sr}_{0.92}\text{Ho}_{0.08}\text{F}_{2.08}$ ($\text{CNC}_{\text{PC}}:2.2$ wt% Ho) are shown in Fig. 4g, h. In these patterns, characteristic diffraction peaks for cellulose I β and $\text{Sr}_{0.92}\text{Ho}_{0.08}\text{F}_{2.08}$ crystalline fluorite phase can easily be seen. A slight difference in the unit cell parameters between the $\text{Sr}_{0.92}\text{Ho}_{0.08}\text{F}_{2.08}$ in the composite film and $\text{Sr}_{0.92}\text{Ho}_{0.08}\text{F}_{2.08}$ powder calcined at 600 °C (Fedorov et al. 2017) was due to the higher annealing temperature of the powder and the possible difference between the real and nominal composition. According to EDX data, the compositions Sr:Ho = 91.38:8.62 (at%) for the CNC_{FP} film: 1.1 wt% Ho and Sr:Ho = 91.83:8.17 (at%) for the CNC_{PC} film: 2.2 wt% Ho were determined. The cellulose crystalline structure did not change after dispersing since the positions of all the reflexes are preserved. However, a slight decrease in the CNC crystallinity index can be noted.

CNC-based composites are homogeneous solid films without cracks with a slightly yellowish color and an average thickness of 25–30 μm . The composite CNC_{AV} film containing 22.3 wt% $\text{Sr}_{0.92}\text{Ho}_{0.08}\text{F}_{2.08}$ (2.2 wt% Ho) and the composite CNC_{PC} film containing 54.5 wt% $\text{Sr}_{0.92}\text{Ho}_{0.08}\text{F}_{2.08}$ (5.4 wt% Ho) are shown in Fig. 11a, b, respectively. The iridescent color of CNC composite films disappeared since they lost their chiral nematic structure. The color of the

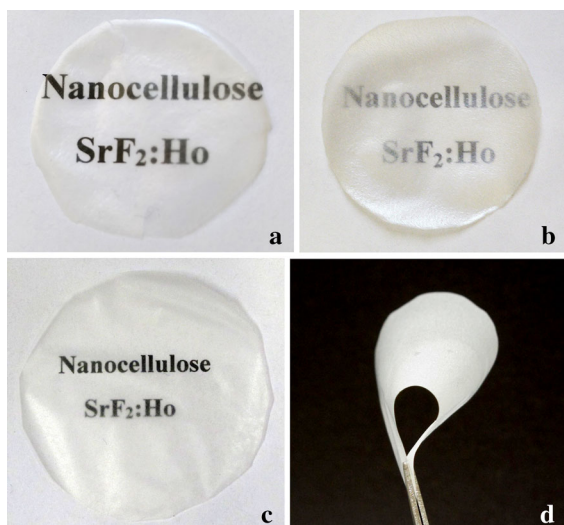


Fig. 11 Composite films appearance: **a** CNC_{AV}/2.2 wt% Ho, **b** CNC_{PC}/5.4 wt% Ho, **c**, **d** CNC_{PC}/CNC_{FP}/5.6 wt% Ho

composite films depends on the up-conversion powder content. Composite CNF-based films were prepared by the solution casting technique with subsequent solvent evaporation under ambient conditions. These films cracked and were damaged with drying or handling; thus, the solution casting technique is not suitable for CNF composite film preparation. For durable and non-wrinkled CNF film preparation, a vacuum filtration method was used followed by drying in a low-pressure oven (Benítez and Walther 2017; Sun et al. 2018). We have prepared flexible, durable and translucent composite films by solution casting technique using 1:1 CNC/CNF dispersions. CNC/CNF:5.6 wt% Ho (45.9 wt% Sr_{0.90}Ho_{0.10}F_{2.10}) composite film is shown in Fig. 11c, d. These photos confirmed the formation of strong, flexible, translucent films without wrinkles.

In order to ensure a uniform distribution of the up-conversion particles in the nanocellulose film, the Sr_{0.92}Ho_{0.08}F_{2.08} or Sr_{0.90}Ho_{0.10}F_{2.10} powders were dispersed in the colloidal CNC suspension by sonication in an ice bath. Then, the CNF dispersion was added and the ultrasonic treatment was continued in an ice bath for another 15 min. SEM images of the so-prepared composite films in topographic contrast (in the secondary electrons mode) (Fig. 12a, e) and in Z-contrast (in the backscattered electrons mode) are shown in Fig. 12b, f.

It should be noted that the surface morphology of a composite film differs significantly from a pure CNC film having a smooth homogeneous structure (Fig. 5a, c, d). The CNC_{PC}:5.4 wt% Ho film has a homogeneous structure with up-conversion particles uniformly distributed over the entire surface and volume. This was confirmed by the Z-contrast of the surface and cross section of the film, (Fig. 12b, d). The particle size of Sr_{1-x}Ho_xF_{2+x} ranged from 50 to 150 nm. EDX analysis data confirmed that Sr/Ho atomic ratio in the composites is very close to that measured in Sr_{0.92}Ho_{0.08}F_{2.08} powders (Fig. S5). Thus, the use of CNC or mixed 1:1 CNC/CNF dispersions made it possible to obtain a composite films with a uniform distribution of up-conversion particles.

The TG and DSC curves demonstrated that the destruction of the CNC_{PC}:2.9 wt% Ho (29.3 wt% Sr_{0.92}Ho_{0.08}F_{2.08}) composite film begins in air at 150 °C (Fig. 8a, b). The exothermic effect at 350 °C corresponded to the oxidation of the organic part of the composite. The exothermal effect at 450 °C corresponded to CO₂ and H₂O formation; the thermal decomposition ended at 538 °C. According to TG data, the residue upon heating up to 800 °C (29.3 wt%) corresponded to the up-conversion powder content in the composite film. CNC/CNF/SrF₂:Ho composite films are even more thermostable, their decomposition began at 170 °C and ended at 550 °C.

One of the most important aspects of nanocellulose composite preparation is the nature of the interactions between its inorganic and polymer components. In the nanocellulose molecule, each monomer unit contains three hydroxyl groups, which can form hydrogen bonds. Inside the CNC, hydroxyl groups participate in the formation of a hydrogen bond network between nanocellulose molecules. We assume that an important role in polymer-inorganic interaction between CNC and SrF₂:Ho particles is a result of hydrogen bond formation at the interphase regions between fluorine ions and primary hydroxyl groups in CNC. This assumption was confirmed by FT-IR spectra (Fig. 9). In the FT-IR spectra of CNC_{PC}/SrF₂ nanocomposite films, the shape of the band at 3350–3450 cm⁻¹ (stretching vibrations of hydroxyl groups involved in the hydrogen bond formation) became narrow, the maximum of the band shifts slightly compared to pure CNC_{PC}. This proved a strong interaction between hydroxyl groups in CNC and fluorine ions in Sr_{1-x}Ho_xF_{2+x} particles with

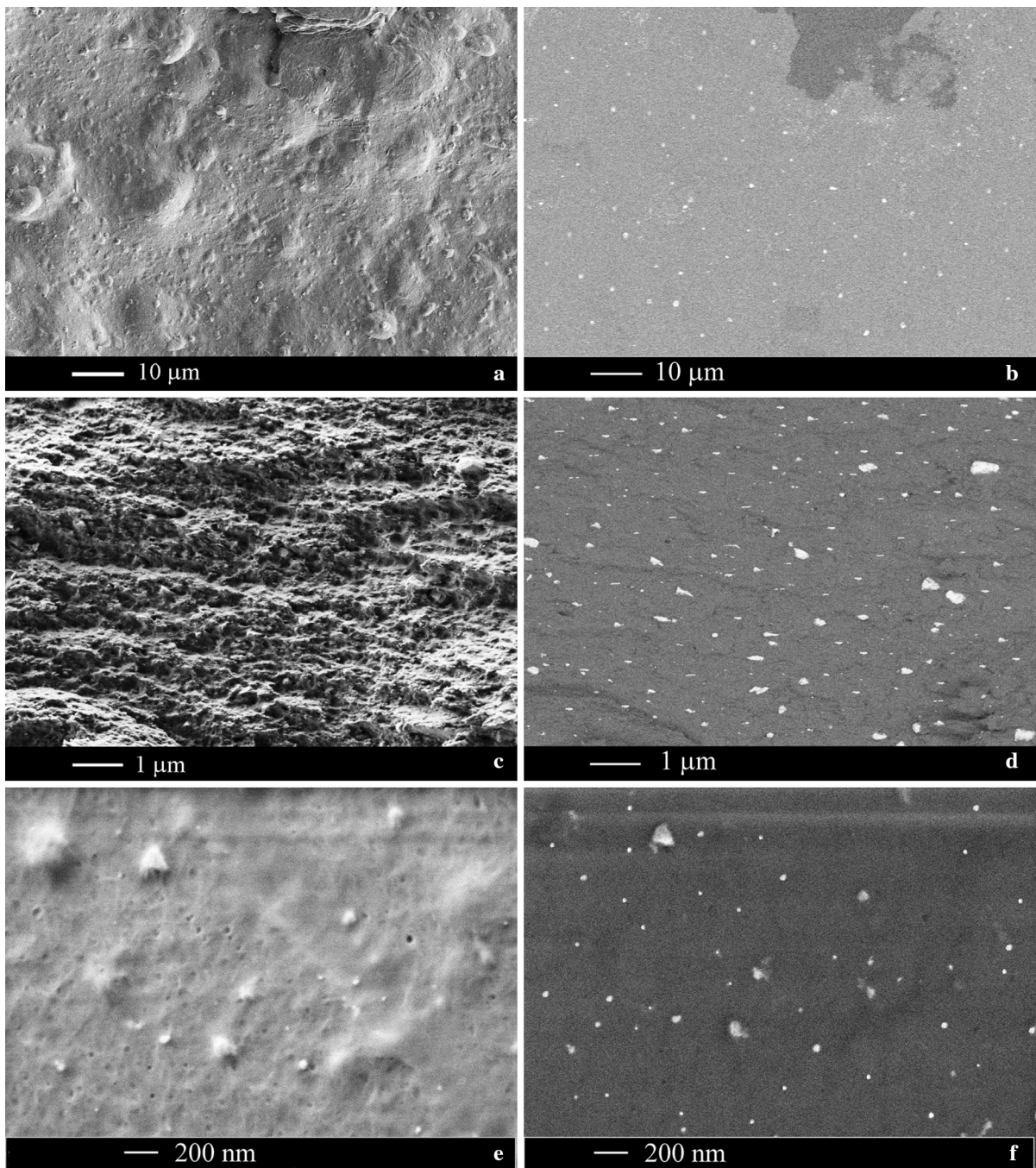


Fig. 12 SEM images of CNC_{PC}/5.4 wt% Ho film in topographic contrast (**a, c, e**), and in Z-contrast (**b, d, f**), cross section of the film (**c, d**)

interfacial hydrogen bonds formation. Schematic presentation of the interfacial hydrogen bonds between OH⁻—groups of nanocellulose and F⁻—

ions of Sr_{1-x}Ho_xF_{2+x} particles was presented in Fig. S6.

The optical transparency of a composite film with up-conversion particles was decreased in comparison

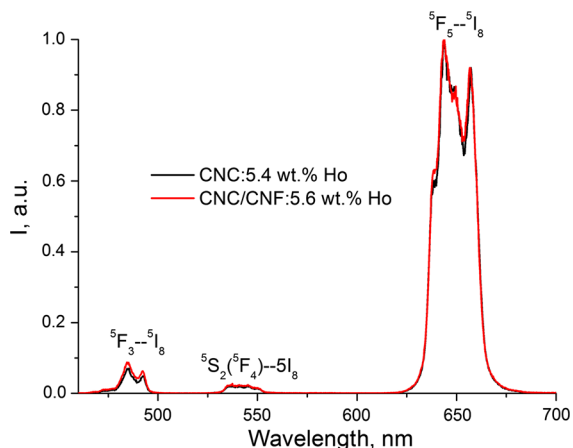


Fig. 13 Up-conversion luminescence spectra of up-conversion cellulose-based films

with CNC films and depends on the $\text{Sr}_{0.92}\text{Ho}_{0.08}\text{F}_{2.08}$ or $\text{Sr}_{0.90}\text{Ho}_{0.10}\text{F}_{2.10}$ concentration in the film. For the CNC_{FP} film with 10.9 wt% $\text{Sr}_{0.92}\text{Ho}_{0.08}\text{F}_{2.08}$ (1.1 wt% Ho), the optical transmission is 44% at 650 nm (Fig. 7f); for 54.5 wt% of $\text{Sr}_{0.92}\text{Ho}_{0.08}\text{F}_{2.08}$ (5.4 wt% Ho) in the CNC_{PC} film the optical transmission is 22%; for 45.9 wt% of $\text{Sr}_{0.90}\text{Ho}_{0.10}\text{F}_{2.10}$ (5.6 wt% Ho) in the $\text{CNC}_{\text{PC}}/\text{CNF}_{\text{FP}}$ film at 650 nm were registered for Fig. 7g, h, respectively. The optical transparency of falls abruptly upon increasing the up-conversion powder content more than 55 wt%. At that level, the films become almost opaque with the loss of their mechanical strength and flexibility.

The luminescence spectra of CNC and 1:1 CNC/CNF composite films with the same amount of holmium and similar luminescence intensity are shown in Fig. 13.

For a composite material processing, it is very important to determine the optimal component stoichiometry. The surface morphology, up-conversion particles distribution, thermal, optical, and luminescent properties of composite films prove that flexible, durable, translucent, up-conversion cellulose-based films can be produced. Mixed 1:1 CNC/CNF dispersions with $\text{Sr}_{0.92}\text{Ho}_{0.08}\text{F}_{2.08}$ or $\text{Sr}_{0.90}\text{Ho}_{0.10}\text{F}_{2.10}$ with the content less than 55 wt% are suitable for excellent quality films preparation.

Conclusions

In the present paper, polymer-inorganic films based on nanocrystalline and nanofibrillated cellulose matrices with $\text{SrF}_2:\text{Ho}$ up-conversion filler powders were prepared for the first time. The influence of nanocellulose properties on the up-conversion films characteristics was determined. The X-ray diffraction data showed that the crystalline structure of nanocellulose and up-conversion particles did not change upon mixing since the positions of all reflections were preserved. The presence of polymer-inorganic interactions between $\text{SrF}_2:\text{Ho}$ particles and cellulose has been confirmed by FT-IR spectroscopy. Hydrogen bond formation played a most important role in composite film stability. Based on SEM/EDX data, the optimal conditions for uniform distribution of $\text{SrF}_2:\text{Ho}$ up-conversion particles in nanocellulose dispersions and films were established. The preparation of homogeneous up-conversion composite films without cracking or film delamination was developed. A 1:1 mixed dispersion of CNC/CNF was shown to be suitable for flexible, durable, translucent, up-conversion composite film production. The spectral and luminescent characteristics of the composite films were investigated. The up-conversion luminescence of CNC/CNF/ $\text{SrF}_2:\text{Ho}$ composite films has been studied in the visible spectral range at $^5\text{I}_7$ level of Ho^{3+} ions pumping. High quality translucent films for photonics applications contain 50–60 wt%, 4–6 wt% Ho in $\text{Sr}_{0.92}\text{Ho}_{0.08}\text{F}_{2.08}$ or $\text{Sr}_{0.90}\text{Ho}_{0.10}\text{F}_{2.10}$ powders. These films can be used for visualization of near-IR laser radiation, as a luminescent labeling for anticounterfeiting, as a luminescent detector, or for other applications.

Acknowledgments We thank Polycell LLC for providing powdered cellulose PCC-0.25 sample and Biokhim LLC for providing Avicel PC105 microcrystalline cellulose sample. The support from Russian Foundation for Basic Research (Grant 16-29-11784-ofi-m) is greatly acknowledged. Authors express their sincere gratitude to Richard L. Simoneaux, and Elena V. Chernova for their most kind assistance in the preparation of the present manuscript and Vladimir N. Kryazhev for polymerization degree analysis.

References

- Abbasi-Moayed S, Golmohammadi H, Hormozi-Nezhad MR (2018) A nanopaper-based artificial tongue: a ratiometric

- fluorescent sensor array on bacterial nanocellulose for chemical discrimination applications. *Nanoscale* 10:2492–2502. <https://doi.org/10.1039/C7NR05801B>
- Abitbol T, Kloser E, Gray DG (2013) Estimation of the surface sulfur content of cellulose nanocrystals prepared by sulfuric acid hydrolysis. *Cellulose* 20:785–794. <https://doi.org/10.1007/s10570-013-9871-0>
- Abitbol T, Rivkin A, Cao Y, Nevo Y, Abraham E, Ben-Shalom T, Lapidot S, Shoseyov O (2016) Nanocellulose, a tiny fiber with huge applications. *Curr Opin Biotechnol* 39:76–88. <https://doi.org/10.1016/j.copbio.2016.01.002>
- Al-Dulaimi AA, Wanrosli W (2017) Isolation and characterization of nanocrystalline cellulose from totally chlorine free oil palm empty fruit bunch pulp. *J Polym Environ* 25:192–202. <https://doi.org/10.1007/s10924-016-0798-z>
- Araki J, Wada M, Kuga S, Okano T (2000) Birefringent glassy phase of a cellulose microcrystal suspension. *Langmuir* 16:2413–2415. <https://doi.org/10.1021/la9911180>
- Auzel F (2004) Upconversion and anti-stokes processes with f and d ions in solids. *Chem Rev* 104:139–174. <https://doi.org/10.1021/cr020357g>
- Beck-Candanedo S, Roman M, Gray D (2005) Effect of conditions on the properties behavior of wood cellulose nanocrystals suspensions. *Biomacromol* 6:1048–1054. <https://doi.org/10.1021/bm049300p>
- Benítez AJ, Walther A (2017) Cellulose nanofibril nanopapers and bioinspired nanocomposites: a review to understand the mechanical property space. *J Mater Chem A* 5:16003–16024. <https://doi.org/10.1039/C7TA02006F>
- Bumbudsanphanroke N, Lee W, Chung U, Ko S (2018) Study of humidity-responsive behavior in chiral nematic cellulose nanocrystal films for colorimetric response. *Cellulose* 25:305–317. <https://doi.org/10.1007/s10570-017-1571-8>
- Cao Y, Jiang Y, Song Y, Cao S, Miao M, Feng X, Fang J, Shi L (2015) Combined bleaching and hydrolysis for isolation of cellulose nanofibrils from waste sackcloth. *Carbohydr Polym* 131:152–158. <https://doi.org/10.1016/j.carbpol.2015.05.063>
- Chen W, Yu H, Liu Y, Chen P, Zhang M, Hai Y (2011) Individualization of cellulose nanofibers from wood using high-intensity ultrasonication combined with chemical pretreatments. *Carbohydr Polym* 83:1804–1811. <https://doi.org/10.1016/j.carbpol.2010.10.040>
- Chu G, Feng J, Wang Y, Zhang X, Xu Y, Zhang H (2014) Chiral nematic mesoporous films of $ZrO_2:Eu^{3+}$: new luminescent materials. *Dalton Trans* 43:15321–15327. <https://doi.org/10.1039/C4DT00662C>
- Chu G, Wang X, Chen T, Xu W, Wang Y, Song H, Xu Y (2015) Chiral electronic transitions of $YVO_4:Eu^{3+}$ nanoparticles in cellulose based photonic materials with circularly polarized excitation. *J Mater Chem C* 3:3384–3390. <https://doi.org/10.1039/C4TC02913E>
- Dai S, Prempeh N, Liu D, Fan Y, Gu M, Chang Y (2017) Cholesteric film of Cu(II)-doped cellulose nanocrystals for colorimetric sensing of ammonia gas. *Carbohydr Polym* 174:531–539. <https://doi.org/10.1016/j.carbpol.2017.06.098>
- Dong S, Roman M (2007) Fluorescently labeled cellulose nanocrystals for bioimaging applications. *J Am Chem Soc* 129:13810–13811
- Dumanli AG, Kamita G, Landman J, van der Kooij H, Glover BJ, Baumberg JJ, Steiner U, Vignolini S (2014) Controlled, bio-inspired self-assembly of cellulose-based chiral reflectors. *Adv Opt Mater* 2:646–650. <https://doi.org/10.1002/adom.201400112>
- Elazzouzi-Hafraoui S, Nishiyama Y, Putaux J-L, Heux L, Dubreuil F, Rochas C (2008) The shape and size distribution of crystalline nanoparticles prepared by acid hydrolysis of native cellulose. *Biomacromol* 9:57–65. <https://doi.org/10.1021/bm700769p>
- Espinosa SC, Kuhnt T, Foster EJ, Weder C (2013) Isolation of thermally stable cellulose nanocrystals by phosphoric acid hydrolysis. *Biomacromol* 14:1223–1230. <https://doi.org/10.1021/bm400219u>
- Eyholzer C, Bordeanu N, Lopez-Suevos F, Rentsch D, Zimmermann T, Oksman K (2010) Preparation and characterization of water-redispersible nanofibrillated cellulose in powder form. *Cellulose* 17:19–30. <https://doi.org/10.1007/s10570-009-9372-3>
- Fedorov PP, Luginina AA, Kuznetsov SV, Osiko VV (2011) Nanofluorides. *J Fluor Chem* 132:1012–1039. <https://doi.org/10.1016/j.jfluchem.2011.06.025>
- Fedorov PP, Luginina AA, Popov AI (2015) Transparent oxyfluoride glass ceramics. *J Fluor Chem* 172:22–50. <https://doi.org/10.1016/j.jfluchem.2015.01.009>
- Fedorov PP, Luginina AA, Rozhnova YA, Kuznetsov SV, Voronov VV, Uvarov OV, Pynenkov AA, Nishchev KN (2017) Preparation of nanodispersed fluorite-type $Sr_{1-x}R_xF_{2+x}$ (R = Er, Yb, Ho) phases from citrate solutions. *J Fluor Chem* 194:8–15. <https://doi.org/10.1016/j.jfluchem.2016.12.003>
- Feng X, Meng X, Zhao J, Miao M, Shi L, Zhang S, Fang J (2015) Extraction and preparation of cellulose nanocrystals from dealginated kelp residue: structures and morphological characterization. *Cellulose* 22:1763–1772. <https://doi.org/10.1007/s10570-015-0617-z>
- Frka-Petesic B, Guidetti G, Kamita G, Vignolini S (2017) Controlling the photonic properties of cholesteric cellulose nanocrystal films with magnets. *Adv Mater* 29:1701469. <https://doi.org/10.1002/adma.201701469>
- Giese M, Blusch LK, Khan MK, MacLachlan M (2015) Functional materials from cellulose-derived liquid crystal templates. *J Angew Chem Int Ed* 54:2888–2910. <https://doi.org/10.1002/anie.201407141>
- Golmohammadi H, Morales-Narváez E, Naghdi T, Merkoçi A (2017) Nanocellulose in sensing and biosensing. *Chem Mater* 29:5426–5446
- Gray DG (2016) Recent advances in chiral nematic structure and iridescent color of cellulose nanocrystal films. *Nanomaterials* 6:213. <https://doi.org/10.3390/nano6110213>
- Gray DG, Mu X (2015) Chiral nematic structure of cellulose nanocrystal suspensions and films; polarized light and atomic force microscopy. *Materials* 8:7873–7888. <https://doi.org/10.3390/ma8115427>
- Grishkewich N, Mohammed N, Tang J, Tam KC (2017) Recent advances in the application of cellulose nanocrystals: a review. *Curr Opin Colloid Interface Sci* 29:32–45. <https://doi.org/10.1016/j.cocis.2017.01.005>
- Gu Z, Yan L, Tain G, Li S, Chai Z, Zhao Y (2013) Recent advances in design and fabrication of upconversion

- nanoparticles and their safe theranostics application. *Adv Mater* 25:3758–3779
- Haase M, Schäfer H (2011) Upconverting nanoparticles. *Angew Chem Int Ed* 50:5808–5829
- Habibi Y (2014) Key advances in the chemical modification of nanocelluloses. *Chem Soc Rev* 43:1519–1542. <https://doi.org/10.1039/c3cs60204d>
- Habibi Y, Lucia LA, Rojas OJ (2010) Cellulose nanocrystals: chemistry, self-assembly, and applications. *Chem Rev* 110:3479–3500. <https://doi.org/10.1021/cr900339w>
- Hamid SBA, Zain SK, Das R, Centi G (2016) Synergic effect of tungstophosphoric acid and sonication for rapid synthesis of crystalline nanocellulose. *Carbohydr Polym* 138:349–355. <https://doi.org/10.1016/j.carbpol.2015.10.023>
- Hassan ML, Fadel SM, Moorefield C, Newkome GR (2014) Dendronized cellulose nanocrystals as templates for preparation of zns and cds quantum dots. *J Macromol Sci A* 51:743–749. <https://doi.org/10.1080/10601325.2014.936296>
- Haywood AD, Davis VF (2017) Effects of liquid crystalline and shear alignment on the optical properties of cellulose nanocrystal films. *Cellulose* 24:705–716. <https://doi.org/10.1007/s10570-016-1150-4>
- Ioelovich MY (2012) Study of cellulose interaction with concentrated solutions of sulfuric acid. *ISRN Chem Eng*. <https://doi.org/10.5402/2012/428974>
- Ioelovich MY (2016) Models of supramolecular structure and properties of cellulose. *Polym Sci Ser A* 58:925–943. <https://doi.org/10.7868/S2308112016060109>
- Ji S, Jang J, Cho E, Kim SH, Kang ES, Kim J, Kim HK, Kong H, Kim SK, Kim JY, Park JU (2017) High dielectric performances of flexible and transparent cellulose hybrid films controlled by multidimensional metal nanostructures. *Adv Mater* 29:1700538. <https://doi.org/10.1002/adma.201700538>
- Jiang H, Zhou D, Qu D, Chu G, Xu W, Song H, Xu Y (2016) Self-organized helical superstructure of photonic cellulose loaded with upconversion nanoparticles showing modulated luminescence. *RSC Adv* 6:76231–76236. <https://doi.org/10.1039/C6RA13894B>
- Jonoobil M, Oladi R, Davoudpour Y, Oksman K, Dufresne A, Hamzeh Y, Davoodi R (2015) Different preparation methods and properties of nanostructured cellulose from various natural resources and residues: a review. *Cellulose* 22:935–969. <https://doi.org/10.1007/s10570-015-0551-0>
- Junka K, Guo J, Filpponen I, Laine J, Rojas OJ (2014) Modification of cellulose nanofibrils with luminescent carbon dots. *Biomacromol* 15:876–881. <https://doi.org/10.1021/bm4017176>
- Kaiser M, Wurth C, Kraft M, Hyppanen I, Soukka T, Resch-Genger U (2017) Power-dependent upconversion quantum yield of NaYF₄:Yb³⁺, Er³⁺ nano- and micrometer-sized particles—measurements and simulations. *Nanoscale* 9:10051–10058. <https://doi.org/10.1039/C7NR02449E>
- Kelly JA, Shopsowitz KE, Ahn JM, Hamad WY, MacLachlan MJ (2012) Chiral nematic stained glass: controlling the optical properties of nanocrystalline cellulose-templated materials. *Langmuir* 28:17256–17262. <https://doi.org/10.1021/la3041902>
- Kim DY, Lee BM, Koo DH, Kang PH, Jeun JP (2016) Preparation of nanocellulose from a kenaf core using E-beam irradiation and acid hydrolysis. *Cellulose* 23:3039–3049. <https://doi.org/10.1007/s10570-016-1037-4>
- Klemm D, Heublein B, Fink H-P, Bohn A (2005) Cellulose: fascinating biopolymer and sustainable raw material. *Angew Chem Int Ed* 44:3358–3393. <https://doi.org/10.1002/anie.200460587>
- Klemm D, Kramer F, Moritz S, Lindstrom T, Ankerfors M, Gray D, Dorris A (2011) Nanocelluloses: a new family of nature-based materials: a review. *Angew Chem Int Edit* 50:5438–5466. <https://doi.org/10.1002/anie.201001273>
- Kuznetsov S, Ermakova Y, Voronov V, Fedorov P, Busko D, Howard IA, Richards BS, Turshatov A (2018) Up-conversion quantum yield of SrF₂:Yb³⁺, Er³⁺ sub-micron particles prepared by precipitation from aqueous solution. *J Mater Chem C* 6:598–604. <https://doi.org/10.1039/c7tc04913g>
- Lavoine N, Desloges I, Dufresne A, Bras J (2012) Microfibrillated cellulose—its barrier properties and applications in cellulosic materials: a review. *Carbohydr Polym* 90:735–764
- Lee BM, Jeun JP, Kang PH, Choi JH, Hong SK (2017) Isolation and characterization of nanocrystalline cellulose from different precursor materials. *Fibers Polym* 18:272–277. <https://doi.org/10.1007/s12221-017-6548-6>
- Li M, Li X, Xiao HN, James TD (2017) Fluorescence sensing with cellulose-based materials. *ChemistryOpen* 6:685–696. <https://doi.org/10.1002/open.201700133>
- Ličen M, Majaron B, Noh J, Schütz C, Bergström L, Lagerwall J, Drevenšek-Olenik I (2016) Correlation between structural properties and iridescent colors of cellulose nanocrystalline films. *Cellulose* 23:3601–3609. <https://doi.org/10.1007/s10570-016-1066-z>
- Lin N, Dufresne A (2014) Nanocellulose in biomedicine: current status and future. *EurPolym J* 59:302–325. <https://doi.org/10.1016/j.eurpolymj.2014.07.025>
- Liu D, Zhong T, Chang PR, Li K, Wu Q (2010) Starch composites reinforced by bamboo cellulosic crystals. *Biores Technol* 101:2529–2536. <https://doi.org/10.1016/j.biortech.2009.11.058>
- Liu D, Wang S, Ma Z, Tian D, Gu M, Lin F (2014) Structure-color mechanism of iridescent cellulose nanocrystal films. *RSC Adv* 4:39322–39331. <https://doi.org/10.1039/c4ra06268j>
- Lyapin AA, Ryabochkina PA, Chabushkin AN, Ushakov SN, Fedorov PP (2015) Investigation of the mechanisms of upconversion luminescence in Ho³⁺ doped CaF₂ crystals and ceramics upon excitation of 5I7 level. *J Lumin* 167:120–125. <https://doi.org/10.1016/j.jlumin.2015.06.01>
- Lyapin AA, Kuznetsov SV, Ryabochkina PA, Merculov AP, Chernov MV, Ermakova YA, Luginina AA, Fedorov PP (2017) Upconversion luminescence of Ca_{1-x}Ho_xF_{2+x} and Sr_{0.98-x}Er_{0.02}Ho_xF_{2.02+x} powders upon excitation by an infrared laser. *Laser Phys Lett* 14:076003
- Magyar A, Hu W, Shanley T, Flatte ME, Hu E, Aharanovich I (2014) Synthesis of luminescent europium defects in diamond. *Nat Commun* 5:3523
- Martins MA, Teixeira EM, Corrêa AC, Ferreira M, Mattoso LHC (2011) Extraction and characterization of cellulose whiskers from commercial cotton fibers. *J Mater Sci*

- 46:7858–7864. <https://doi.org/10.1007/s10853-011-5767-2>
- Miao M, Zhao J, Feng X, Cao Y, Cao S, Zhao Y, Ge X, Sun L, Shi L, Fang J (2015) Fast fabrication of transparent and multi-luminescent TEMPO-oxidized nanofibrillated cellulose nanopaper functionalized with lanthanide complexes. *J Mater Chem C* 3:2511–2517. <https://doi.org/10.1039/C4TC02622E>
- Mondal S (2017) Preparation, properties and applications of nanocellulosic materials. *Carbohydr Polym* 163:301–316. <https://doi.org/10.1016/j.carbpol.2016.12.050>
- Montanar S, Roumani M, Heux L, Vignon MR (2005) Topochemistry of carboxylated cellulose nanocrystals resulting from TEMPO-mediated oxidation. *Macromolecules* 38:1665–1671. <https://doi.org/10.1021/ma048396c>
- Moon RJ, Schueneman GT, Simonsen J (2016) Overview of cellulose nanomaterials, their capabilities and applications. *JOM* 68:2383–2394. <https://doi.org/10.1007/s11837-016-2018-7>
- Morales-Narváez E, Golmohammadi H, Naghdi T, Yousefi H, Kostiv U, Horák D, Pourreza N, Merkoçi A (2015) Nanopaper as an optical sensing platform. *ACS Nano* 9:7296–7305
- Mu X, Gray DG (2014) Formation of chiral nematic films from cellulose nanocrystal suspensions is a two-stage process. *Langmuir* 30:9256–9260. <https://doi.org/10.1021/la501741r>
- Naderi A (2017) Nanofibrillated cellulose: properties reinvestigated. *Cellulose* 24:1933–1945. <https://doi.org/10.1007/s10570-017-1258-1>
- Nam S, French AD, Condon BD, Concha M (2016) Segal crystallinity index revisited by the simulation of X-ray diffraction patterns of cotton cellulose Ib and cellulose II. *Carbohydr Polym* 135:1–9. <https://doi.org/10.1016/j.carbpol.2015.08.035>
- Nedilko M, Alekseev O, Chornii V, Kovalov K, Lazarenko M, Nedilko S, Scherbatskyi V, Boyko V, Sheludko V (2018) Structure and properties of microcrystalline cellulose “ceramics-like” composites incorporated with LaVO₄:Sm oxide compound. *Acta Phys Pol A* 133:838–842. <https://doi.org/10.12693/APhysPolA.131.838>
- Neto WPF, Putaux JL, Mariano M, Ogawa Y, Otaguro H, Pasquinia D, Dufresne A (2016) Comprehensive morphological and structural investigation of cellulose I and II nanocrystals prepared by sulphuric acid hydrolysis. *RSC Adv* 6:76017–76027. <https://doi.org/10.1039/C6RA16295A>
- Nguyen TD, Hamad WY, MacLachlan MJ (2017) Near-IR-sensitive upconverting nanostructured photonic cellulose films. *Adv Opt Mater* 5:1600514. <https://doi.org/10.1002/adom.201600514>
- Nishiyama Y, Langan P, Chanzy H (2002) Crystal structure and hydrogen-bonding system in cellulose I β from synchrotron X-ray and neutron fiber diffraction. *J Am Chem Soc* 124:9074–9082. <https://doi.org/10.1021/ja0257319>
- Niu F, Li M, Huang Q, Zhang X, Pan W, Yang J, Li J (2017) The characteristic and dispersion stability of nanocellulose produced by mixed acid hydrolysis and ultrasonic assistance. *Carbohydr Polym* 165:197–204. <https://doi.org/10.1016/j.carbpol.2017.02.048>
- Oguzlu H, Danumah C, Boluk Y (2017) Colloidal behavior of aqueous cellulose nanocrystal suspensions. *Curr Opin Colloid Interface Sci COCIS* 29:46–56. <https://doi.org/10.1016/j.cocis.2017.02.002>
- Pak AM, Ermakova JA, Kuznetsov SV, Ryabova AV, Pominova DV, Voronov VV (2017) Efficient visible range SrF₂:Yb:Er- and SrF₂:Yb:Tm-based up-conversion lumino-phores. *J Fluor Chem* 194:16–22. <https://doi.org/10.1016/j.jfluchem.2016.12.002>
- Pan J, Hamad W, Straus SK (2010) Parameters affecting the chiral nematic phase of nanocrystalline cellulose films. *Macromolecules* 43:3851–3858. <https://doi.org/10.1021/ma902383k>
- Park JH, Noh JH, Schütz C, Salazar-Alvarez G, Scalia G, Bergström L, Lagerwall JFP (2014) Macroscopic control of helix orientation in films dried from cholesteric liquid-crystalline cellulose nanocrystal suspensions. *Chem-PhysChem* 15:1477–1484. <https://doi.org/10.1002/cphc.201400062>
- Parker RM, Guidetti G, Williams CA, Zhao T, Narkevicius A, Vignolini S, Frka-Petesic B (2017) The self-assembly of cellulose nanocrystals: hierarchical design of visual appearance. *Adv Mater* 29:1704477. <https://doi.org/10.1002/adma.201704477>
- Qing Y, Sabo R, Wu Y, Zhu JY, Cai Z (2015) Self-assembled optically transparent cellulose nanofibril films: effect of nanofibril morphology and drying procedure. *Cellulose* 22:1091–1102. <https://doi.org/10.1007/s10570-015-0563-9>
- Querejeta-Fernandez A, Kopera B, Prado KS, Klinkova A, Methot M, Chauve G, Bouchard J, Helmy AS, Kumacheva E (2015) Circular dichroism of chiral nematic films of cellulose nanocrystals loaded with plasmonic nanoparticles. *ACS Nano* 9:10377–10385. <https://doi.org/10.1021/acsnano.5b04552>
- Querejeta-Fernández A, Chauve G, Metho M, Bouchard J, Kumacheva E (2014) Chiral plasmonic films formed by gold nanorods and cellulose nanocrystals. *J Am Chem Soc* 136:4788–4793. <https://doi.org/10.1021/ja501642p>
- Revol JF, Godbout L, Gray DG (1998) Solid self-assembled films of cellulose with chiral nematic order and optically variable properties. *J Pulp Paper Sci* 24:146–149
- Ritter B, Krahl T, Scholz G, Kemnitz E (2016) Local structures of solid solutions Sr_{1-x}Y_xF_{2+x} (x = 0...0.5) with fluorite structure prepared by sol-gel and mechanochemical syntheses. *J Phys Chem C* 120:8992–8999. <https://doi.org/10.1021/acs.jpcc.6b01834>
- Rozhnova YA, Luginina AA, Voronov VV, Ermakov RP, Kuznetsov SV, Ryabova AV, Pominova DV, Arbenina VV, Osiko VV, Fedorov PP (2014) White light lumino-phores based on Yb³⁺/Er³⁺/Tm³⁺-coactivated strontium fluoride powders. *Mater Chem Phys* 148:201–207
- Rozhnova YA, Kuznetsov SV, Luginina AA, Voronov VV, Ryabova AV, Pominova DV, Ermakov RP, Usachev VA, Kononenko NE, Baranchikov AE, Ivanov VK, Fedorov PP (2016) New Sr_{1-x-z}R_x(NH₄)_zF_{2+x-z} (R = Yb, Er) solid solution as precursor for high efficiency up-conversion lumino-phor and optical ceramics on the base of strontium fluoride. *Mater Chem Phys* 172:150–157. <https://doi.org/10.1016/j.matchemphys.2016.01.055>

- Salas C, Nypelö T, Rodriguez-Abreu C, Carrillo C, Rojas OJ (2014) Nanocellulose properties and applications in colloids and interfaces. *Curr Opin Colloid Interface Sci* COCIS 19:383–396. <https://doi.org/10.1016/j.cocis.2014.10.003>
- Sedov VS, Kuznetsov SV, Ralchenko VG, Mayakova MN, Krivobok VS, Savin SS, Martyanov AK, Romanishkin ID, Khomich AA, Fedorov PP, Konov VI (2017) Diamond-EuF₃ nanocomposites with bright orange photoluminescence. *Diam Relat Mater* 72:47–52. <https://doi.org/10.1016/j.diamond.2016.12.022>
- Shanmugam K, Doosthosseini H, Varanasi S, Garnier G, Batchelor W (2018) Flexible spray coating process for smooth nanocellulose film production. *Cellulose* 25:1725–1741. <https://doi.org/10.1007/s10570-018-1677-7>
- Shopsowitz KE, Hamad WY, MacLachlan MJ (2011) Chiral nematic mesoporous carbon derived from nanocrystalline cellulose. *J Angew Chem Int Ed* 50:10991–10995. <https://doi.org/10.1002/anie.201105479>
- Shopsowitz KE, Stahl A, Hamad WY, MacLachlan MJ (2012) Hard templating of nanocrystalline titanium dioxide with chiral nematic ordering. *J Angew Chem Int Ed* 51:6886–6890. <https://doi.org/10.1002/anie.201201113>
- Siro I, Plackett D (2010) Microfibrillated cellulose and new nanocomposite materials: a review. *Cellulose* 17:459–494. <https://doi.org/10.1007/s10570-010-9405-y>
- Sirviö JA, Visanko M, Liimatainen H (2016) Acidic deep eutectic solvents as hydrolytic media for cellulose nanocrystal production. *Biomacromol* 17:3025–3032. <https://doi.org/10.1021/acs.biomac.6b00910>
- Sun B, Zhang M, Hou Q, Liu R, Wu T, Si C (2016) Further characterization of cellulose nanocrystal (CNC) preparation from sulfuric acid hydrolysis of cotton fibers. *Cellulose* 23:439–450. <https://doi.org/10.1007/s10570-015-0803-z>
- Sun X, Wu Q, Zhang X, Ren S, Lei T, Li W, Xu G, Zhang Q (2018) Zhang Nanocellulose films with combined cellulose nanofibers and nanocrystals: tailored thermal, optical and mechanical properties. *Cellulose* 25:1103–1115. <https://doi.org/10.1007/s10570-017-1627-9>
- Tardy BL, Ago M, Guo J, Borghei M, Kämäräinen T, Rojas OJ (2017) Optical properties of self-assembled cellulose nanocrystals films suspended at planar-symmetrical interfaces. *Small* 13:1702084. <https://doi.org/10.1002/sml.201702084>
- Vicente AT, Araújo A, Mendes MJ, Nunes D, Oliveira MJ, Sanchez-Sobrado O, Ferreira MP, Águas H, Fortunato E, Martins R (2018) Multifunctional cellulose-paper for light harvesting and smart sensing applications. *J Mater Chem C* 6:3143–3181. <https://doi.org/10.1039/C7TC05271E>
- Wilts BD, Dumanli AG, Middleton R, Vukusic P, Vignolini S (2017) Chiral optics of helicoidal cellulose nanocrystal films. *APL Photonics* 2:040801. <https://doi.org/10.1063/1.4978387>
- Wu CN, Yang Q, Takeuchi M, Saito T, Isogai A (2014) Highly tough and transparent layered composites of nanocellulose and synthetic silicate. *Nanoscale* 6:392–399. <https://doi.org/10.1039/C3NR04102F>
- Xue J, Song F, Yin X, Wang X, Wang Y (2015) Let it shine: a transparent and photoluminescent foldable nanocellulose/quantum dot paper. *ACS Appl Mater Interfaces* 7:10076–10079. <https://doi.org/10.1021/acsami.5b02011>
- Xue B, Zhang Z, Sun Y, Wang J, Jiang H, Du M, Chi C, Li X (2018) Near-infrared emissive lanthanide hybridized nanofibrillated cellulose nanopaper as ultraviolet filter. *Carbohydr Polym* 186:176–183. <https://doi.org/10.1016/j.carbpol.2017.12.088>
- Yagoub MYA, Swart HC, Noto LL, O’Connell JH, Lee ME, Coetsee E (2014) The effects of Eu-concentrations on the luminescent properties of SrF₂: Eu nanophosphor. *J Lumin* 156:150–156. <https://doi.org/10.1016/j.jlumin.2014.08.014>
- Yagoub MYA, Swart HC, Coetsee E (2015) Concentration quenching, surface and spectral analyses of SrF₂:Pr³⁺ prepared by different synthesis techniques. *Opt Mat* 42:204–209. <https://doi.org/10.1016/j.optmat.2015.01.011>
- Zeng JH, Su J, Li ZH, Yan RX, Li YD (2005) Synthesis and upconversion luminescence of hexagonal-phase NaY-F₄:Yb, Er³⁺, phosphors of controlled size and morphology. *Adv Mater* 17:2119–2123
- Zhang Z, Chang H, Xue B, Han Q, Lü X, Zhang S, Li X, Zhu X, Wong W, Li K (2017) New transparent flexible nanopaper as ultraviolet filter based on red emissive Eu(III) nanofibrillated cellulose. *Opt Mat* 73:747–753. <https://doi.org/10.1016/j.optmat.2017.09.039>
- Zhang L, Lyu S, Chen Z, Wang S (2018) Fabrication flexible and luminescent nanofibrillated cellulose films with modified SrAl₂O₄: Eu, Dy phosphors via nanoscale silica and aminosilane. *Nanomaterials* 8:352–366. <https://doi.org/10.3390/nano8050352>
- Zhao J, Wei Z, Feng X, Miao M, Sun L, Cao S, Shi L, Fang J (2014) Luminescent and transparent nanopaper based on rare-earth up-converting nanoparticles grafted nanofibrillated cellulose derived from garlic skin. *ACS Appl Mater Interfaces* 6:14945–14951. <https://doi.org/10.1021/am5026352>
- Zor E (2018) Silver nanoparticles-embedded nanopaper as a colorimetric chiral sensing platform. *Talanta* 184:149–155. <https://doi.org/10.1016/j.talanta.2018.02.096>
- Zor E, SabriAlpaydin S, Arici A, Muhammed EsadSaglam ME, Bingol H (2018) Photoluminescentnanopaper-based microcuvette for iodide detection in seawater. *Sens Actuators B Chem* 254:1216–1224. <https://doi.org/10.1016/j.snb.2017.07.208>